

1 **A Multiscale Model of Partial Melts 2: Numerical** 2 **Results**

G. Simpson

3 Department of Mathematics, University of Toronto, Toronto, Ontario,
4 Canada.

M. Spiegelman

5 Department of Applied Physics and Applied Mathematics, Columbia
6 University, New York, New York, USA

M. I. Weinstein

7 Department of Applied Physics and Applied Mathematics, Columbia
8 University, New York, New York, USA

G. Simpson, Department of Mathematics, University of Toronto, Toronto, ON M5S 2E4,
Canada. (simpson@math.toronto.edu)

M. Spiegelman, Department of Applied Physics and Applied Mathematics, Columbia Univer-
sity, New York, NY 10027, USA. Lamont-Doherty Earth Observatory, Palisades, NY 10964, USA.
(mspieg@ldeo.columbia.edu)

M. I. Weinstein, Department of Applied Physics and Applied Mathematics, Columbia Univer-
sity, 200 Mudd, New York, NY 10027, USA. (miw2103@columbia.edu)

9 **Abstract.** In a companion paper, equations for partially molten media
10 were derived using two-scale homogenization theory. This approach begins
11 with a grain scale description and then coarsens it through multiple scale ex-
12 pansions into a macroscopic model. One advantage of homogenization is that
13 effective material properties, such as permeability and the shear and bulk
14 viscosity of the two-phase medium, are characterized by *cell problems*, bound-
15 ary value problems posed on a representative microstructural cell. The so-
16 lutions of these problems can be averaged to obtain macroscopic parameters
17 that are consistent with a given microstructure. This is particularly impor-
18 tant for estimating the “compaction length” which depends on the product
19 of permeability and bulk viscosity and is the intrinsic length scale for vis-
20 cously deformable two-phase flow.

21 In this paper, we numerically solve ensembles of cell problems for several
22 geometries. We begin with simple intersecting tubes as this is a one param-
23 eter family of problems with well known results for permeability. Using this
24 data, we estimate relationships between the porosity and all of the effective
25 parameters with curve fitting. For this problem, permeability scales as ϕ^n ,
26 $n \sim 2 - 3$, as expected and the bulk viscosity scales as ϕ^{-m} , $m \sim 1$, which
27 has been speculated, but never shown directly for deformable porous media.
28 The second set of cell problems add spherical inclusions at the tube inter-
29 sections. These show that the permeability is controlled by the smallest pore
30 throats and not by the total porosity, as expected. The bulk viscosity remains
31 inversely proportional to the porosity, and we conjecture that this quantity

32 is insensitive to the specific microstructure. The computational machinery
33 developed can be applied to more general geometries, such as texturally equi-
34 librated pore shapes. However, we suspect that the qualitative behavior of
35 our simplified models persists in these more realistic structures. In partic-
36 ular, our hybrid numerical–analytical model predicts that for purely mechan-
37 ical coupling at the microscale, all homogenized models will have a compaction
38 length that vanishes as porosity goes to zero. This has implications for com-
39 putational models, and it suggests that these models might not resist com-
40 plete compaction.

1. Introduction

41 Partially molten regions in the Earth’s asthenosphere (e.g. beneath mid-ocean ridges or
42 subduction zones) are usually modeled as a viscously deformable permeable media. Such
43 models are typically composed of macroscopic equations for the conservation of mass,
44 momentum and energy of each phase. In our companion paper, *Simpson et al.* [2008a],
45 we derived several systems of governing equations for partially molten systems using
46 homogenization. Briefly, we began with a grain scale description of two interpenetrating
47 fluids, each satisfying the Stokes equations, coupled by their common interface. Several
48 different macroscopic models could then be coarsened from this microscopic description,
49 depending on our assumptions on the velocities, viscosities, and grain scale geometry.

50 An important feature of this approach is that macroscopic properties such as perme-
51 ability, shear viscosity, and bulk viscosity naturally appear in the macroscopic equations,
52 even if they are not defined at the grain scale. In particular, permeability and bulk vis-
53 cosity are properties of the two-phase aggregate, not the volume averages of small scale
54 variations. In contrast, previous work on the magma problem, including *McKenzie* [1984];
55 *Bercovici and Ricard* [2003, 2005]; *Bercovici* [2007]; *Hier-Majumder et al.* [2006]; *Ricard*
56 [2007], began with models much larger than the grain scale. There, the viscosities, per-
57 meability, and other closures were assumed and justified from other results. In contrast,
58 homogenization derives these properties self-consistently.

59 While homogenization techniques appropriately inserts the constitutive relationships
60 into the macroscopic equations, connecting them to the microstructure requires the solu-
61 tion of specific “cell problems.” For the physical system derived in *Simpson et al.* [2008a],

62 there are actually a series of ten Stokes problems for both fluid and solid posed on the
 63 micro-scale (which can be reduced to four for micro-structures with sufficient symmetry).

In this paper, we numerically explore the cell problems to extract parameterizations of the various effective parameters in terms of porosity, a simple measurement of the microstructure. A feature of this work is to derive constitutive relationships for the bulk viscosity as a function of porosity, which is essential for describing compactible permeable media. In particular, we show that for a range of simple pore structure the effective bulk viscosity is related to the porosity as.

$$\zeta_{\text{eff.}} \propto \phi^{-1}$$

64 Our results and some additional theory suggest that this scaling is insensitive to the
 65 specific pore geometry.

Since permeability and bulk-viscosity can both be consistently related to the same microstructure, these calculations also allow us to study the “compaction length” [McKenzie, 1984]. At sufficiently low melt concentrations, it is approximately

$$\delta_{\text{comp.}} \propto \sqrt{k_{\text{eff.}} \zeta_{\text{eff.}}}$$

which depends on the product of the derived permeability $k_{\text{eff.}}$ and bulk viscosity $\zeta_{\text{eff.}}$, both of which depend on the porosity. The compaction length is the intrinsic length scale in magma dynamics. This work suggests that under solely mechanical deformation,

$$\lim_{\phi \rightarrow 0} \delta_{\text{comp.}}(\phi) = 0,$$

66 implying that no mechanical mechanism prevents a region from compacting to zero poros-
 67 ity. This result also places strong resolution constraints on computational models of
 68 magma migration which may require a regularization for small porosities.

69 An outline of this work is as follows. In Section 2, we review several models of partially
 70 molten rock and highlight the constitutive relations. In Section 3, we demonstrate the
 71 process of assuming a cell geometry to extract computational closures for the macroscopic
 72 system. We revisit these closures in Section 4 for more general geometries to assess their
 73 robustness. Finally, in Section 5, we combine our numerics with the equations and examine
 74 the implications.

2. Review of Equations and Constitutive Relations

2.1. Macroscopic Equations

In *Simpson et al.* [2008a], we showcased three models for momentum conservation in a partially molten medium. They were distinguished by the assumed scalings for the relative velocities and viscosities between the fluid and solid phases, along with the connectivity of the pore network. One of them, dubbed Biphase-I, was given by the equations:

$$0 = \bar{\rho}\mathbf{g} - \nabla P + \nabla \left[\left(\zeta_{\text{eff.}} - \frac{2}{3}\mu_s(1 - \phi) \right) \nabla \cdot \mathbf{V}^s \right] \quad (1a)$$

$$+ \nabla \cdot [2(1 - \phi)\mu_s e(\mathbf{V}^s)] + \nabla \cdot [2\eta_{\text{eff.}}^{lm} e_{lm}(\mathbf{V}^s)]$$

$$\phi(\mathbf{V}^f - \mathbf{V}^s) = -\frac{k_{\text{eff.}}}{\mu_f} (\nabla P - \mathbf{g}^f) \quad (1b)$$

$$\nabla \cdot [\phi\mathbf{V}^f + (1 - \phi)\mathbf{V}^s] = 0 \quad (1c)$$

75 Notation for his model may be found in Table 1. In particular, $k_{\text{eff.}}$ and $\zeta_{\text{eff.}}$ are the
 76 emergent permeability and bulk viscosity. $\eta_{\text{eff.}}$ is an auxiliary, tensorial, shear viscosity
 77 capturing grain scale anisotropy. All are related to the aforementioned cell problems.
 78 We highlight this case because (1a – 1c) is nearly identical to the models of McKenzie,
 79 Bercovici, Ricard, and others in the absence of melting and surface physics.

2.2. Constitutive Relations

80 The constitutive relations for the permeability and viscosity are fundamental to the
 81 dynamics of these models. Indeed, they are the source of much nonlinearity and it is
 82 useful to review some proposed closures. Notation for this appears in Table 2.

83 At low porosity, it is common to relate permeability, κ , to porosity by a power law,
 84 $\kappa \propto \phi^n$. Estimates of n vary, $n \sim 2 - 5$, *Scheidegger* [1974]; *Bear* [1988]; *Dullien* [1992];
 85 *Turcotte and Schubert* [2002]; *McKenzie* [1984]; *Doyen* [1988]; *Cheadle* [1989]; *Martys*
 86 *et al.* [1994]; *Faul et al.* [1994]; *Faul* [1997, 2000]; *Koponen et al.* [1997]; *Wark and Watson*
 87 [1998]; *Wark et al.* [2003]; *Cheadle et al.* [2004]. For partially molten rocks, the exponent
 88 is better constrained by both analysis and experiment to $n \sim 2 - 3$.

For the matrix shear viscosity, *Hirth and Kohlstedt* [1995a, b]; *Kohlstedt et al.* [2000];
Kelemen et al. [1997]; *Kohlstedt* [2007] experimentally observed a melt weakening effect,
 which they fit to the curve:

$$\mu_{s+f} = \mu_s \exp(-\phi/\phi_*), \quad \phi_* = O(10^{-2}) \quad (2)$$

89 μ_{s+f} is the shear viscosity of the solid matrix in the presence of melt; μ_s is the shear
 90 viscosity a melt-free matrix. In *Bercovici et al.* [2001]; *Bercovici and Ricard* [2003] and
 91 related works, the viscosity is weighted by $(1 - \phi)$, which is also present in (1a). Reiterat-
 92 ing, μ_{s+f} is a fitting of experimental data. Regardless, the shear viscosity is taken to be
 93 isotropic, and porosity weakening in other models.

94 Lastly, the bulk viscosity, ζ_s , is often taken as $\zeta_s \propto \phi^{-m}$, $m \sim 0 - 1$, though m is usually
 95 either zero or one. $m = 0$ has often been used because the variation of bulk viscosity
 96 with porosity is poorly constrained by observations. *Scott and Stevenson* [1984] and oth-
 97 ers invoked the bore hole studies of ice by *Nye* [1953] to justify $m = 1$. In that work,
 98 Nye considered the dynamics of individual spherical and cylindrical voids in an infinite

99 medium. *Taylor* [1954]; *Prud'homme and Bird* [1978] computed $m = 1$, in the limit of
 100 small porosity, using models of incompressible fluids mixed with gas bubbles. *Schmelting*
 101 [2000] also employed $\zeta_s \propto \phi^{-1}$, citing studies for the analogous question of the effective
 102 bulk modulus of a fluid filled poroelastic medium. Those results rely on the self-consistent
 103 approximation methodology, treated in *Torquato* [2002]. Models in *Bercovici et al.* [2001];
 104 *Bercovici and Ricard* [2003] and related works possess a ϕ^{-1} term that functions as a
 105 bulk viscosity, though it has a very different origin. *McKenzie* [1984] suggested using a
 106 metallurgical model of spheres due to *Arzt et al.* [1983] which considered a range of mech-
 107 anisms for densification of powders under hot isostatic pressing. For viscous compaction
 108 mechanisms, the Arzt result recover a bulk viscosity proportional to ϕ^{-1} for Newtonian
 109 viscosities. However, for very small porosities, they suggest that surface diffusion effects
 110 become important and imply that $\zeta_s \propto \log(\phi^{-1})$. Finally, *Connolly and Podladchikov*
 111 [1998] invoke an asymmetric bulk viscosity that is weaker during expansion than during
 112 compaction, which is motivated by the deformation of brittle crustal materials. However,
 113 it is unclear if this rheology is relevant to high-temperature/high-pressure creeping ma-
 114 terials as are expected in the mantle. In general, it is expected that the bulk-viscosity
 115 should become unbounded as the porosity reduces to zero as the system then becomes
 116 incompressible.

2.3. Cell Problems

117 In homogenization, a medium with fine scale features is modeled by introducing two or
 118 more spatial scales. As discussed in *Simpson et al.* [2008a], the direct approach makes
 119 multiple scale expansions of the dependent variables, letting them depend on both the
 120 coarse and fine length scales.

The two characteristic lengths in our model are L , the macroscopic scale, and ℓ , the grain scale. Their ratio,

$$\epsilon = \frac{\ell}{L}$$

121 is the parameter in which we perform the multiple scale expansions. In the process of
 122 performing the expansions and matching powers of ϵ , we are mathematically constrained
 123 to solve a collection of auxiliary cell problems posed on the fine scale. Notation for this
 124 setup is provided in Table 3.

125 It is analytically advantageous to approximate the mixture as a periodic medium; such
 126 a configuration appears in Figure 1. Ω , the macroscopic region containing both matrix
 127 and melt is periodically tiled with scaled copies of the cell, scaled to unity in Figure 2.
 128 The cell problems are posed within Y_s , the matrix portion of the cell, and Y_f , the melt
 129 portion for the cell. Y_s and Y_f meet on interface γ .

Generically, the cell problems take the form:

$$\nabla_y \cdot (-pI + 2e_y(\mathbf{v})) = \mathbf{f} \quad \text{in } Y_f \text{ or } Y_s \quad (3a)$$

$$\nabla_y \cdot \mathbf{v} = g \quad \text{in } Y_f \text{ or } Y_s \quad (3b)$$

$$(-pI + 2e_y(\mathbf{v})) \cdot \mathbf{n} = \boldsymbol{\tau} \cdot \mathbf{n} \quad \text{or} \quad \mathbf{u} = \mathbf{U} \quad \text{on } \gamma \quad (3c)$$

130 which are generally, compressible Stokes flow problems for the microscopic solid and melt
 131 velocities and pressures (\mathbf{v}, p) . Here, ∇_y is the gradient, $\nabla_y \cdot$ is the divergence, and e_y
 132 the strain-rate operator defined on the fine length scale y . A more complete description
 133 is given in *Simpson et al.* [2008a]. \mathbf{f} , g , $\boldsymbol{\tau}$, and \mathbf{U} are prescribed forcing functions on the
 134 relevant portion of Y , either Y_s or Y_f . The solution, (\mathbf{v}, p) , is periodic on the portion of
 135 the boundary not intersecting the interface γ . The cell problems may be interpreted as

136 the fine scale response to an applied stress on a unit cell of either the melt or the matrix.
137 The material parameters – k_{eff} , ζ_{eff} , and η_{eff} . – are then defined as the cell average of an
138 appropriate manipulation of these pressures and velocities defined at the pore scale. In
139 particular, an average of the solid pressure in one problem determines the bulk viscosity
140 and certain averages of melt velocities in another problem determine the permeability.
141 Again, we emphasize that the material parameters are not volume averages of the same
142 parameters at the fine scale.

3. Effective Parameters: Intersecting Tube Geometry

143 To connect the effective material properties – η_{eff} , k_{eff} , and ζ_{eff} . – with the porosity,
144 we must solve the cell problems and extract a parameterization. Unfortunately, the so-
145 lution of the Stokes equations in a generic three dimensional domain lacks an analytic
146 representation. Thus we compute the solutions to the cell problems numerically and fit
147 the results to appropriate parameterized constitutive models. Notation for this section is
148 summarized in Table 4.

149 As a first example of numerically closing the constitutive relations in a homogenization
150 based model, we study the cell domain of triply intersecting cylinders, pictured in Figure
151 3. The fluid occupies the cylinders while the solid is the complementary portion of the
152 cube. While this geometry is an oversimplification of real pore-geometries, it serves as
153 proof of concept of the unified, self-consistent homogenization algorithm. Additionally, it
154 serves as a numerical check since the permeability for this problem is expected to scale as
155 ϕ^2 . In Section 4 we examine a generalization of this geometry.

156 In what follows, we emphasize that the information given by the parameterizations
 157 should be read with a certain skepticism. The order of magnitude and signs of the coeffi-
 158 cients and exponents are of greater utility than the particular numbers.

We remark here that for the intersecting tube geometry, the tube radius scaled to the cell-size, b , can be explicitly related to the porosity:

$$\phi = 3\pi b^2 - 8\sqrt{2}b^3 \quad (4)$$

159 We solve our problems using finite elements on unstructured meshes using the open
 160 source libraries from the FEniCS and PETSc projects [e.g. *Dupont et al.*, 2003; *Kirby and*
 161 *Logg*, 2007; *Logg*, 2007; *Balay et al.*, 2004, 2001], with meshes generated using CUBIT
 162 [*Sandia Corporation*, 2008]. Details of this method and numerical benchmarks are given
 163 in Appendix B.

3.1. Effective Permeability

The first cell problem we treat is for permeability. The equations are:

$$-\nabla_y q^i + \nabla_y^2 \mathbf{k}^i = -\mathbf{e}_i \quad \text{in } Y_f \quad (5a)$$

$$\nabla_y \cdot \mathbf{k}^i = 0 \quad \text{in } Y_f \quad (5b)$$

$$\mathbf{k}^i = 0 \quad \text{on } \gamma \quad (5c)$$

where \mathbf{k}^i is a three-dimensional velocity and q^i is a scalar pressure, for each $i = 1, 2, 3$.

These are equations (64a – 64c) in *Simpson et al.* [2008a] and describe the motion of the melt through the porous matrix. In general, the permeability is the second order tensor:

$$\langle K \rangle_f = \left[\int_{Y_f} \mathbf{k}^1 dy \quad \int_{Y_f} \mathbf{k}^2 dy \quad \int_{Y_f} \mathbf{k}^3 dy \right]$$

The symmetry properties of the domain simplify this to:

$$\langle K \rangle_f = \langle \mathbf{k}_1^1 \rangle_f I, \quad \mathbf{k}_1^1 \text{ is the first component of vector } \mathbf{k}^1$$

Thus, it is sufficient to compute the case $i = 1$. Then k_{eff} , the permeability of the matrix, in (1b) is

$$\boxed{k_{\text{eff.}} \equiv \langle \mathbf{k}_1^1 \rangle_f} \quad (6)$$

164 Darcy's Law and permeability have been studied by many techniques, including ho-
 165 mogenization; we refer the reader to the references in Section 2.2. We study it here to
 166 understand how the permeability behaves *in concert* with the other constitutive relations
 167 as the microstructure varies. This also serves as a benchmark problem for our software;
 168 see Appendix B.

As noted, porosity and permeability are often related by a power law, $\kappa \propto \phi^n$, with $n \sim 2-5$. To motivate such a relation, we turn to a toy model, as presented in *Turcotte and Schubert* [2002]. The melt is assumed to be in Poiseuille flow through triply intersecting cylinders. Additionally, the cylinders have small radii; it is a low porosity model. The permeability of such a system is

$$\kappa_{\text{toy-I}} = \frac{\ell^2 \phi^2}{72\pi} \approx 0.0044 \ell^2 \phi^2. \quad (7)$$

169 Other simple models are developed in *Scheidegger* [1974]; *Bear* [1988]; *Dullien* [1992].

We now fit our computed permeabilities, $\langle \mathbf{k}_1^1 \rangle_f$, to porosity by such a relation. For the tube domains, the least squares fit is

$$\langle \mathbf{k}_1^1 \rangle_f = \exp(-4.42 \pm .105) \phi^{2.20 \pm .0391}. \quad (8)$$

170 This curve and the data appear in Figure 4. The fit matches expectations of an $O(10^{-3} -$
 171 $10^{-2})$ prefactor and an exponent $\sim 2-3$. The error in (8) is the associated 95% confidence

172 interval. We report these intervals in all regressions, though they rely on the specious
 173 assumption that error in our synthetic data is normally distributed.

3.2. Effective Bulk Viscosity

The effective bulk viscosity is related to the solution $(\bar{\xi}, \zeta)$ of:

$$\nabla_y \cdot (-\zeta I + 2e_y(\bar{\xi})) = 0 \quad \text{in } Y_s \quad (9a)$$

$$\nabla_y \cdot \bar{\xi} = 1 \quad \text{in } Y_s \quad (9b)$$

$$(-\zeta I + 2e_y(\bar{\xi})) \cdot \mathbf{n} = 0 \quad \text{on } \gamma \quad (9c)$$

where $\bar{\xi}$ is a three-dimensional velocity and ζ is a scalar pressure. These are equations (B1a – B1c) in *Simpson et al.* [2008a] and are associated with the compaction of the matrix. The effective bulk viscosity is then defined as

$$\zeta_{\text{eff.}} \equiv \mu_s \langle \zeta \rangle_s - \frac{2}{3} \mu_s (1 - \phi) \quad (10)$$

174 The dependence of the effective bulk viscosity of partially molten rock as a function of
 175 porosity is the most poorly constrained of the material properties. This is partly due to
 176 the difficulties in constructing an experiment that will measure it as a function of porosity
 177 independently of the shear viscosity *McKenzie* [1984]; *Kelemen et al.* [1997]; *Stevenson*
 178 *and Scott* [1991]. As mentioned in Section 2.2, a bulk viscosity $\propto \phi^{-1}$ has often appeared
 179 in the literature.

Two toy models for the bulk viscosity of an incompressible fluid seeded with compressible gas bubbles were formulated by *Taylor* [1954]; *Prud'homme and Bird* [1978]. They

relate the bulk viscosity to the porosity as:

$$\zeta_s = \frac{4}{3} \frac{\mu_s}{\phi} \quad \text{Taylor} \quad (11a)$$

$$\zeta_s = \frac{4}{3} \frac{\mu_s}{\phi} (1 - \phi) \quad \text{Prud'homme and Bird} \quad (11b)$$

180 Taylor's expression, (11a), relied on a single inclusion model for a gas bubble in an infinite
 181 medium. (11b) is derived by considering a sphere of fluid with a gas filled spherical cavity,
 182 and seeking the bulk viscosity of a compressible fluid that will give rise to the same
 183 radial stress for specified boundary motion. The $1 - \phi$ is due to Prud'homme and Bird
 184 restricting their model to a finite volume. This factor also appears in the proposed bulk
 185 viscosity of *Schmeling* [2000]. These expressions have motivated the use of $\zeta_s \propto \phi^{-1}$ in
 186 macroscopic models of partial melts, although they actually arise from a different problem
 187 of a compressible inclusion in an incompressible fluid, rather than the divergent flow of two
 188 interconnected incompressible fluids. Surprisingly, when we consider a simple toy problem
 189 to approximate the the full cell calculation, we find that the expressions are identical.

Appendix A provides details of this toy problem, which is related to equations (9a – 9c), and gives the solution

$$\langle \zeta \rangle_s = \frac{4}{3\phi} \left(1 + \frac{\phi}{2} \right) (1 - \phi),$$

from which we get

$$\zeta_{\text{eff.}} = \frac{4\mu_s}{3\phi} (1 - \phi).$$

This motivates trying to numerically fit $\langle \zeta \rangle_s$ to $(1 - \phi)^p / \phi^q$, expecting p and q to be close to unity. Indeed, the data, plotted in Figure 5, fits the curve

$$\langle \zeta \rangle_s = \exp(-0.131 \pm 0.00514) \phi^{-1.02 \pm 0.00132} (1 - \phi)^{0.884 \pm 0.00869} \quad (12)$$

190 which is quite similar to the scaling of the toy model.

3.3. Supplementary Anisotropic Viscosity

We now examine the cell problem related to the supplementary viscosity $\eta_{\text{eff.}}$, a fourth order tensor. The equations are:

$$\nabla_y \cdot (-\pi^{lm} I + 2e_y(\bar{\chi}^{lm})) = 0 \quad \text{in } Y_s \quad (13a)$$

$$\nabla_y \cdot \bar{\chi}^{lm} = 0 \quad \text{in } Y_s \quad (13b)$$

$$(-\pi^{lm} \delta_{ij} + 2e_{y,ij}(\bar{\chi}^{lm})) n_j = -\frac{1}{2} (\delta_{il} \delta_{jm} + \delta_{im} \delta_{jl}) n_j \quad \text{on } \gamma \quad (13c)$$

where $\bar{\chi}^{lm}$ is a three-dimensional velocity vector and π^{lm} is a scalar pressure, *for each pair* (l, m) , $l = 1, 2, 3$ and $m = 1, 2, 3$. These are equations (B2a – B2c) from *Simpson et al.* [2008a] and are tied to tensorial surface stresses applied on the matrix. Using the solutions $(\bar{\chi}^{lm}, \pi^{lm})$,

$$\boxed{\eta_{\text{eff.}}^{lm} \equiv \langle e_y(\bar{\chi}^{lm}) \rangle_s} \quad (14)$$

191 Because of symmetry, we need only consider two problems: $(l, m) = (1, 1)$ and $(l, m) =$
 192 $(1, 2)$, corresponding to normal stress and shear stress in each direction.

Although we have no toy problem as motivation, $\phi^p(1 - \phi)^q$ proved to be satisfactory. First, we study the problem $(l, m) = (1, 1)$, a uniaxial stress problem. For the tubes, we fit

$$-\langle e_{1,1}(\bar{\chi}^{11}) \rangle_s = \exp(-1.72 \pm .0405) \phi^{.964 \pm .0104} (1 - \phi)^{1.23 \pm .0685} \quad (15)$$

193 This vanishes as $\phi \rightarrow 0$ and as $\phi \rightarrow 1$ and it is nearly linear at small porosity. The curves
 194 and the data are plotted in Figure 6.

There is also the simple shear stress problem, $(l, m) = (1, 2)$. For this, we fit

$$-\langle e_{12}(\bar{\chi}^{(12)}) \rangle_s = \exp(-1.04 \pm .0188) \phi^{1.06 \pm .00485} (1 - \phi)^{1.17 \pm .0318} \quad (16)$$

195 Plots for this are given in Figure 7.

196 We could now employ the simple computational closures (8), (12), (15), and (16), in
 197 (1a – 1c), to simulate and study the macroscopic problem.

4. Generalization of the Cell Domains

198 Regrettably, Earth materials are not as trivial as intersecting cylinders. Even an ide-
 199 alized olivine grain is a tetrakaidekahedron, pictured in Figures 8. As depicted, some
 200 fraction of the melt lies along the triple junctions and some is at the quadruple junc-
 201 tions. Other examples of idealized, texturally equilibrated arrangements appear in *von*
 202 *Bargen and Waff* [1986] and *Cheadle* [1989]; *Cheadle et al.* [2004]. These methods are also
 203 amenable to studying *random* media. One could compute relations based on ensembles
 204 of randomly generated cell domains, solving all relevant cell problems on the ensemble.

Motivated by Figure 8, we explore a simple generalization of the tube geometry by adding a sphere of independent radius at the intersection, as in Figure 9. This retains the symmetry of the previous model, but adds a second parameter, allowing multiple geometries for the same porosity. The sphere captures some aspect of the pocket at the quadruple junctions. The sphere radius, a , and the tube radius, b , are related to the porosity by the equation:

$$\phi = \pi \left[-4a^3 + 4a^2\sqrt{a^2 - b^2} + b^2 \left(3 - 4\sqrt{a^2 - b^2} \right) + \frac{4}{3}a^3 \right] \quad (17)$$

205 We shall refer to it as the *sphere+tube* geometry.

206 We now repeat the computations of Section 3 on the sphere+tube geometry to assess
 207 the sensitivity of the effective parameters to cell geometry. We also perform computations
 208 on domains where the fluid occupies an isolated sphere at the center of a cube. Though
 209 this is disconnected, it provides useful information.

4.1. Permeability Revisited

210 Parameterizing the porosity-permeability relation for this generalization is quite chal-
 211 lenging. In contrast to the tube geometry, the data points of the sphere+tube geometry,
 212 plotted in Figure 4, do not collapse onto a curve. There is some positive correlation be-
 213 tween permeability and porosity, and for a given porosity, the permeability of the equiv-
 214 alent tube geometry is an upper bound.

215 To better understand the trend, we examine the computed flow fields in Figures 10
 216 and 11. These plot the velocity magnitude on two fluid domains with the same tube
 217 size, but different sphere sizes. Most of the flow is within the tube. While there is some
 218 detrainment as it enters the sphere, the flow in the tube appears insensitive to the size of
 219 the sphere.

This motivates fitting permeability against tube radius. Indeed, an alternative to (7),
 is

$$k_{\text{toy-II}} = \frac{\delta^4}{128\ell^2} \quad (18)$$

The tube diameter δ , is equivalent to $2b$, b the the tube radius in the tube and sphere+tube
 geometries. Both data sets appear in Figure 12. This is a significant improvement over
 Figure 4. The least square fits are:

$$\langle \mathbf{k}_1^1 \rangle_f = \exp(-0.592 \pm .0354)b^{4.10 \pm .0156}, \quad \text{for tube geometry} \quad (19)$$

$$\langle \mathbf{k}_1^1 \rangle_f = \exp(-0.628 \pm .198)b^{3.93 \pm .0684}, \quad \text{for sphere+tube geometry} \quad (20)$$

220 These estimates with (18); taking $\delta = 2b$ and scaling out ℓ , this relationship is $k_{\text{toy-II}} =$
 221 $.125b^4$. The data is still positively correlated with sphere radius, altering it by as as much
 222 as an order of magnitude. The deviations are greatest when both $b \ll 1$ and $b \ll a$.

223 That the permeability is more strongly correlated with the tube radius than the overall
 224 geometry is not surprising. *Koponen et al.* [1997] discuss the notion of effective porosity,
 225 the portion of the void space where there is significant flow. Denoting our effective porosity
 226 $\phi_{\text{eff.}}$, we seek a relation $k_{\text{eff.}} \propto \phi_{\text{eff.}}^n$.

Given the flow fields in Figures 10 and 11 and the success with the tube radius fittings,
 we posit that the effective porosity is the portion of the porosity within the tubes. A two-
 dimensional analog appears in Figure 13. Using (8), we define $\phi_{\text{eff.}}$ for the sphere+tube
 domains:

$$\phi_{\text{eff.}} = 3\pi b^2 - 8\sqrt{2}b^3 \quad (21)$$

227 *Zhu and Hirth* [2003] made a similar approximation; from *von Barga and Waff* [1986]
 228 they construed that the permeability was controlled by the minimal cross-sectional area
 229 of the pore network. A similar argument is made by *Cheadle* [1989]. In our domains, the
 230 minimal cross-sectional area is πb^2 .

We fit

$$\langle \mathbf{k}_1^1 \rangle_f = \exp(-4.44 \pm .144) \phi_{\text{eff.}}^{2.06 \pm .0374} \quad \text{for sphere+tube.} \quad (22)$$

231 This appears in Figure 14. Again, deviation is highest for very large spheres with very
 232 thin tubes. Unfortunately, $\phi_{\text{eff.}}$ does not satisfy a conservation law, making it a less than
 233 ideal macroscopic quantity to track, though it does satisfy the bound $\phi_{\text{eff.}} \leq \phi$.

There is still as much as an order of magnitude deviation at low porosity from relation
 (22). The unresolved part of the permeability for the $\phi_{\text{eff.}}$ fit is increasing in the sphere
 radius. This motivates trying to fit against both $\phi_{\text{eff.}}$ and another parameter. It is sufficient
 to fit permeability to $\phi_{\text{eff.}}$ and ϕ , resulting in

$$\langle \mathbf{k}_1^1 \rangle_f = \exp(-4.20 \pm .0681) \phi_{\text{eff.}}^{1.88 \pm .0229} \phi^{.351 \pm .0300} \quad \text{for sphere+tube.} \quad (23)$$

This is plotted in Figure 15. Some deviation persists at low porosity, but it is less than an order of magnitude. Both the sphere+tube data points and the tube data points collapse onto this curve. (23) is also consistent with (8), the fit of porosity against permeability for the tube geometry. Taking $\phi_{\text{eff.}} = \phi$ for the tubes, (23) becomes

$$\langle \mathbf{k}_1^1 \rangle_f = \exp(-4.20)\phi^{2.23} \quad (24)$$

This is similar to the most general permeability relationships, formulated in *Scheidegger* [1974]; *Bear* [1988]:

$$\text{permeability} = \ell^2 f_1(\text{pore shape}) f_2(\phi) \quad (25)$$

234 By including both ϕ and $\phi_{\text{eff.}}$ in (23), we capture some aspect of the pore shape.

4.2. Bulk and Supplementary Viscosities Revisited

In contrast to the permeability problem, the effective bulk viscosity and supplementary anisotropic viscosity are quite robust to the domain distortion. As before, we fit $\langle \zeta \rangle_s$ to $(1 - \phi)^p / \phi^q$, expecting p and q to be close to unity. For the sphere+tube and the sphere geometry, the least squares fits are:

$$\langle \zeta \rangle_s = \exp(0.301 \pm 0.0102)\phi^{-1.00 \pm 0.00174}(1 - \phi)^{0.718 \pm 0.0337}, \quad \text{for sphere geometry} \quad (26a)$$

$$\langle \zeta \rangle_s = \exp(0.124 \pm 0.0975)\phi^{-0.985 \pm 0.0252}(1 - \phi)^{1.09 \pm 0.186}, \quad \text{for sphere+tube geometry} \quad (26b)$$

235 The data and these fits are plotted appear in Figure 5. The spherical geometry appears
 236 to be an upper bound on the bulk viscosity for a given porosity. We also remark that the
 237 prefactors vary by less than an order of magnitude amongst the different domains. This
 238 is a strong endorsement of an effective bulk viscosity $\propto \phi^{-1}$ not only for small porosity,
 239 but also for moderate porosities $\gtrsim 10\%$.

The supplementary anisotropic viscosity terms are also robust under this geometric perturbation. For the problem $(l, m) = (1, 1)$, the two new geometries fit:

$$-\langle e_{1,1}(\bar{\chi}^{11}) \rangle_s = \exp(-1.68 \pm .0588)\phi^{.980 \pm .0101}(1 - \phi)^{3.56 \pm .195}, \quad \text{for sphere geometry} \quad (27a)$$

$$-\langle e_{1,1}(\bar{\chi}^{11}) \rangle_s = \exp(-1.94 \pm .139)\phi^{.912 \pm .0359}(1 - \phi)^{1.25 \pm .265}, \quad \text{for sphere+tube geometry} \quad (27b)$$

240 The curves and the data are also plotted in Figure 6. For $\phi \lesssim 10\%$, the spread amongst
241 the three geometries is less than an order of magnitude.

Similar results are found in the $(l, m) = (1, 2)$ problem. The two new additional domains are fit with:

$$-\langle e_{12}(\bar{\chi}^{(12)}) \rangle_s = \exp(-1.67 \pm .0222)\phi^{1.02 \pm .000380}(1 - \phi)^{0.400 \pm .0737}, \quad \text{for sphere geometry} \quad (28a)$$

$$-\langle e_{12}(\bar{\chi}^{(12)}) \rangle_s = \exp(-1.32 \pm .00883)\phi^{1.03 \pm .00228}(1 - \phi)^{0.871 \pm .169}, \quad \text{for sphere+tube geometry} \quad (28b)$$

242 The sphere+tube data is bounded between the sphere data and the tube data; the spread
243 is less than an order of magnitude.

5. Discussion and Open Problems

244 We have successfully parameterized the macroscopic parameters on ensemble of domains
245 for the simple pore geometries. These can now be consistently used with the macroscopic
246 model given by equations (1a – 1c). We now review and discuss our computations, both
247 independently of and together with the macroscopic equations.

5.1. Sensitivity to Geometry

248 As demonstrated by our computations in Sections 3 and 4, the effective parameters
249 demonstrate a variety of sensitivities to the geometry. Permeability, for our cell geome-
250 tries, can be bounded by porosity, $k_{\text{eff.}} \lesssim \phi^n$, where $n \sim 2$, as seen in Figure 4. But in

251 general, it cannot be expressed as a function of a single parameter, such as porosity. How-
252 ever, if the shapes are constrained by textural equilibration, as in *Cheadle* [1989], there
253 will be a single variable parameterization for each dihedral angle. Solving the cell prob-
254 lems on these shapes, and assessing their sensitivity to the dihedral angle, is an important
255 open problem.

256 In contrast, the bulk viscosity appears to be rather insensitive to the geometry, scaling
257 as $\zeta_{\text{eff.}} \propto \phi^{-1}(1 - \phi)$. We see this from the variation, or lack thereof, between the data
258 and fits for the isolated spheres and the triply intersecting cylinders, in Figure 5. Though
259 these are entirely different geometric structures, there is less than an order of magnitude of
260 variation in the computed $\zeta_{\text{eff.}}$. These too merit computation on the texturally equilibrated
261 shapes. Randomly generated geometries may also be of interest.

262 Both components of the supplementary anisotropic shear viscosity appear to be insen-
263 sitive to geometry, with less than an order of magnitude amongst the three geometries.
264 However, because the problems are driven by surface stresses, it may be that a more
265 anisotropic shape could alter these scalings. Studying them on randomly generated shapes
266 may provide insight on the role of grain scale anisotropy.

5.2. Bulk Viscosity

267 Perhaps our most significant result is the self-consistent bulk viscosity, arising from
268 a *purely mechanical model* of partially molten rock. A spatially varying bulk viscosity
269 is quite important. Indeed, significant differences in dynamics were noted between the
270 solutions of the *McKenzie* [1984] model and the model in *Ricard et al.* [2001]. The authors
271 point to the use of a constant bulk viscosity in the McKenzie model as the source of the
272 discrepancy.

273 Prior to *Ricard et al.* [2001], *Schmeling* [2000] remarked that the ϕ^{-1} dependence has
 274 an important impact on the compaction length. For $\phi = O(1\%)$, the bulk viscosity is two
 275 orders of magnitude greater than the shear viscosity. While many studies took ζ_s and μ_s
 276 to be the same order, this higher bulk viscosity leads to a compaction length an order of
 277 magnitude greater. *Ricard* [2007] made a similar observation on the impact of variable
 278 bulk viscosity on the compaction length.

279 *Schmeling* also commented that this variable bulk viscosity could induce melt focusing
 280 towards the axis in his plume simulations. This is an additional nonlinearity that may
 281 be important to geophysical problems. Many studies relying on the McKenzie model
 282 employed a constant bulk viscosity, including *Richter and McKenzie* [1984]; *Spiegelman*
 283 *and McKenzie* [1987]; *Spiegelman* [1993a, b, c]; *Aharonov et al.* [1997]; *Spiegelman* [1996];
 284 *Kelemen et al.* [1997]; *Spiegelman et al.* [2001]; *Katz et al.* [2004]; *Spiegelman et al.* [2007].
 285 *Spiegelman and Kelemen* [2003]; *Spiegelman* [2003] used a bulk viscosity, with $\zeta_s \propto \phi^{-m}$
 286 with $m > n$, n the exponent in the permeability relationship $\kappa \propto \phi^n$ to prevent the system
 287 from compacting to zero between the reactive channels. It would be interesting to revisit
 288 these problems with a ϕ^{-1} bulk viscosity.

5.3. Compaction Length

We now combine (1a – 1c), our leading order equations derived by multiple scale ex-
 pansions, with our computed constitutive relations. For $\phi \ll 1$ our numerical estimates,

(23), (26a–26b), (15–27b), (27a), and (16–28a) are approximately:

$$\zeta_{\text{eff.}} \approx \mu_s \zeta_0 \phi^{-1} (1 - \phi)$$

$$\eta_{\text{eff.}} \approx \mu_s \eta_0 \phi (1 - \phi)$$

$$k_{\text{eff.}} \approx k_0 \ell^2 \phi_{\text{eff.}}^{1.9} \phi^{.35}$$

k_0 is a $O(10^{-3} - 10^{-2})$ constant, ζ_0 is an $O(1)$ constant, and η_0 is a $O(10^{-1})$ constant fourth order tensor. Under these assumptions, the equations for the Biphasic-I model, (1a – 1c), simplify:

$$\begin{aligned} 0 = & \bar{\rho} \mathbf{g} - \nabla P + \nabla [\mu_s \zeta_0 \phi^{-1} \nabla \cdot \mathbf{V}^s] \\ & + \nabla \cdot \left[2(1 - \phi) \mu_s e(\mathbf{V}^s) - \frac{2}{3} (1 - \phi) \mu_s \nabla \cdot \mathbf{V}^s I \right] \end{aligned} \quad (29)$$

$$\begin{aligned} & + \nabla \cdot [2\mu_s \phi (1 - \phi) \eta_0^{lm} e_{x,lm}(\mathbf{V}^s)] \\ \phi(\mathbf{V}^f - \mathbf{V}^s) = & - \frac{k_0 \ell^2 \phi_{\text{eff.}}^{1.9} \phi^{.35}}{\mu_f} (\nabla P - \mathbf{g}^f) \end{aligned} \quad (30)$$

$$\nabla \cdot [\phi \mathbf{V}^f + (1 - \phi) \mathbf{V}^s] = 0 \quad (31)$$

If we were to use these equations and numerically derived constitutive relations to solve a boundary value problem, the compaction length would again appear as an important length scale,

$$\begin{aligned} \delta_{\text{comp.}} &= \sqrt{\frac{[\zeta_{\text{eff.}} + \frac{4}{3} \mu_s (1 - \phi) + 2 |\eta_{\text{eff.}}|] k_{\text{eff.}}}{\mu_f}} \\ &\approx \ell \sqrt{\frac{\mu_s (1 - \phi) (\zeta_0 \phi^{-1} + \frac{4}{3} + 2 |\eta_0| \phi) k_0 \phi_{\text{eff.}}^{1.9} \phi^{.35}}{\mu_f}} \end{aligned}$$

If $\phi \ll 1$, then $\zeta_0 \phi^{-1} \gg 4/3 + 2 |\eta_0| \phi$ and $1 - \phi \approx 1$,

$$\delta_{\text{comp.}} \approx \ell \sqrt{\zeta_0 k_0 \mu_s / \mu_f} \phi^{-.325} \phi_{\text{eff.}}^{.95} \quad (32)$$

Since $\phi_{\text{eff.}} \leq \phi$, we have an upper bound on the compaction length,

$$\delta_{\text{comp.}} \lesssim \ell \sqrt{\zeta_0 k_0 \mu_s / \mu_f} \phi^{.6} \quad (33)$$

Hence,

$$\lim_{\phi \rightarrow 0} \delta_{\text{comp.}} = 0$$

289 We believe (33), which constrains the compaction length by the porosity raised to a small
 290 positive power, is relatively insensitive to the geometric configuration. This follows from
 291 our alleged robustness of our effective bulk viscosity, $\zeta_{\text{eff.}} \propto \phi^{-1}$, and the broad agreement
 292 in the porosity–permeability relationship, $\kappa \propto \phi^n$ with $n \geq 2$.

293 A compaction length that vanishes with porosity has interesting consequences. For
 294 example, this compaction length scaling does not rule out the possibility that a partially
 295 molten rock could expel all fluid by mechanical means. It also does not permit the
 296 infiltration of fluid into a dry region. Understanding how any of these systems of equations
 297 transition between a partially molten region and a dry region is an outstanding question.
 298 We also note that though our scaling relationship does not forbid compaction, it does
 299 not imply it either. There may be a dynamic response that prevents the matrix from
 300 mechanically compacting to zero. Such effects were mathematically proven to exist in a
 301 one-dimensional simplification of the model, without melting or freezing, in *Simpson et al.*
 302 [2007]; *Simpson and Weinstein* [2008]; *Simpson et al.* [2008c].

303 If, instead, we had concluded $\delta_{\text{comp.}} \propto \phi^q$, with $q < 0$, then the compaction length
 304 would become unbounded as the melt vanished. Hence the region of deformation in the
 305 matrix needed to segregate additional fluid would also become infinite, precluding further
 306 segregation solely by mechanical processes.

Because we have parameterized the permeability with $\phi_{\text{eff.}}$, we can explicitly see the re-
 sponse of the compaction length as the melt network becomes disconnected. $\phi_{\text{eff.}}$ measures
 the volume fraction where melt flows. As the channels close up and the melt becomes

trapped and $\phi_{\text{eff.}} \rightarrow 0$. Taking this limit in (32),

$$\lim_{\phi_{\text{eff.}} \rightarrow 0} \delta_{\text{comp.}} = 0$$

The compaction length can vanish, *even if the melt fraction remains bounded away from zero*. A similar conclusion could be drawn for the compaction length of McKenzie,

$$\delta_{\text{M84}} = \sqrt{\frac{\kappa(1 - \phi)(\zeta_s + \frac{4}{3}\mu_s)}{\mu_f}} \quad (34)$$

307 Letting $\kappa = \kappa_0\phi^n$, if we interpret the loss of connectivity as $\kappa_0 \rightarrow 0$, δ_{M84} vanishes with
 308 nonzero porosity.

5.4. Other Physics

309 There are several results that were not realized by our model, and these merit discus-
 310 sion. We did not recover the $\zeta_s \propto \log(\phi^{-1})$ result of *Arzt et al.* [1983]. This arises in
 311 the limit of sufficiently low porosity that the primary transport mechanism is by grain
 312 boundary diffusion. Since we did not include any surface physics in our fine scale model,
 313 we should not have expected to upscale their effects. If good grain scale descriptions of
 314 these processes could be formulated, it might be possible to coarsen them via homog-
 315 enization, perhaps recovering this macroscopic relation. However, as $\log(\phi^{-1})$ becomes
 316 unbounded more slowly than ϕ^{-1} , this result does not change the basic argument about
 317 the compaction length vanishing with zero porosity.

Another relationship not captured by either our work is the experimental fit for matrix shear viscosity in the presence of melt from *Hirth and Kohlstedt* [1995a, b]; *Kelemen et al.* [1997]; *Kohlstedt et al.* [2000]; *Kohlstedt* [2007],

$$\mu_{s+f} \propto \exp(-\phi/\phi_*)$$

318 Our model possesses a porosity weakening mechanism; all of the viscosity terms are \propto
319 $1 - \phi$. However, the anisotropic part, η_{eff} , is not sign definite and is small compared
320 to the isotropic component. Furthermore, there does not appear to be an exponential
321 relation. *Hirth and Kohlstedt* [1995a] hypothesized that the presence of melt enhances
322 grain boundary diffusion, providing a fast path for deformation through the melt. As
323 with the $\log(\phi^{-1})$ bulk viscosity, this is a surface physics phenomenon not captured by
324 our Stokes models.

5.5. Open Problems

325 As discussed, two important open problems are the computation of the cell problems
326 on more realistic and general cell domains and the inclusion of surface physics into the
327 model. The former problem is rather straightforward, requiring good computational tools
328 for generating the domains and solving the Stokes equations on them. The latter problem
329 is more challenging, requiring fine scale equations for these processes.

330 The models could also be augmented by giving the matrix a nonlinear rheology, leading
331 to nonlinear cell problems. Though these could be solved and studied numerically, this
332 is much more difficult as the different forcing components no longer decouple. Rather
333 than being able to split the matrix cell problems into a bulk viscosity problem, and two
334 surface stress problems, they would have to be done simultaneously. However, the derived
335 parameterizations for the effective viscosities would be important to magma migration.
336 A nonlinear matrix rheology is expected at large strain rates and was needed to compu-
337 tationally model physical experiments for shear bands in *Katz et al.* [2006].

338 Another important physical rheology is viscoelasticity. *Connolly and Podladchikov*
339 [1998]; *Vasilyev et al.* [1998] extended the earlier, purely viscous, models to include elastic

340 effects. This is an important regime since it permits both short and long time scales, as
 341 is found at the asthenosphere-lithosphere boundary.

Appendix A: Spherical Model

Here we develop a toy model for equations (9a – 9c),

$$\nabla_y \cdot (-\zeta I + 2e_y(\bar{\xi})) = 0 \quad \text{in } Y_s$$

$$\nabla_y \cdot \bar{\xi} = 1 \quad \text{in } Y_s$$

$$(-\zeta I + 2e_y(\bar{\xi})) \cdot \mathbf{n} = 0 \quad \text{on } \gamma$$

whose solution yields the effective bulk viscosity,

$$\zeta_{\text{eff.}} = \mu_s \langle \zeta \rangle_s - \frac{2}{3} \mu_s (1 - \phi)$$

Consider a fluid domain, Y_f , occupying a small isolated sphere at the center of the unit cube; Y_s is the complementary region. Smoothing out the exterior boundary of Y_s deforms it into a sphere. We solve the dilation stress problem on this domain. To avoid confusion, let

$$Y_s^{\text{sphere}} = \{ \mathbf{y} \in \mathbb{R}^3 \mid a \leq |\mathbf{y}| \leq 1 \} \tag{A1}$$

$$Y_s^{\text{cube}} = \left\{ \mathbf{y} \in \left[-\frac{1}{2}, \frac{1}{2} \right]^3 \mid |\mathbf{y}| \geq a \right\} \tag{A2}$$

342 Our toy problem is posed on Y_s^{sphere} .

Although periodicity is no longer a meaningful boundary condition, it can be shown that the normal velocity on the periodic part of ∂Y_s vanishes. We set the normal velocity to zero on the exterior boundary of Y_s^{sphere} . On the interior shell, the stress free condition

remains. The equations are:

$$\nabla \cdot (-\zeta I + 2e(\bar{\xi})) = 0 \quad \text{in } Y_s^{\text{sphere}} \quad (\text{A3a})$$

$$\nabla \cdot \bar{\xi} = 1 \quad \text{in } Y_s^{\text{sphere}} \quad (\text{A3b})$$

$$(-\zeta I + 2e(\bar{\xi})) \cdot \mathbf{n} = 0 \quad \text{at } r = a \quad (\text{A3c})$$

$$\bar{\xi} \cdot \mathbf{n} = 0 \quad \text{at } r = 1 \quad (\text{A3d})$$

$a < 1$ is the radius of the interior sphere. Decomposing the velocity into incompressible, $\mathbf{v}^{\text{inc.}}$, and compressible, $\nabla \Pi$, components, the compressible part solves:

$$\nabla^2 \Pi = 1 \quad (\text{A4})$$

Let the boundary conditions on the potential be:

$$\Pi|_{r=a} = 0, \quad \nabla \Pi|_{r=1} = 0 \quad (\text{A5})$$

Since the problem is spherically symmetric, its solution is

$$\Pi = \frac{1}{6}(r^2 - a^2) + \frac{1}{3}(r^{-1} - a^{-1}) \quad (\text{A6})$$

The incompressible velocity must be divergence free. Again, by spherical symmetry,

$$\nabla \cdot \mathbf{v}^{\text{inc.}} = \frac{1}{r^2} \partial_r (r^2 v_r^{\text{inc.}}) = 0 \Rightarrow v_r^{\text{inc.}} = C/r^2$$

To satisfy the boundary condition at $r = 1$, $\mathbf{v}^{\text{inc.}} \cdot \mathbf{n} = v_r^{\text{inc.}} = 0$. Therefore, $C = 0$ and $\mathbf{v}^{\text{inc.}} = 0$. The pressure then solves $\partial_r \zeta = 0$, so it is constant,

$$\zeta(r) = \zeta(a) \quad \text{for } r \in (a, 1)$$

Applying boundary condition (A3c),

$$\zeta = 2e_{rr}(\bar{\xi})|_{r=a} = 2\partial_r^2 \Pi|_{r=a} = \frac{1}{3} \left(2 + \frac{4}{a^3} \right)$$

In this geometry, $\phi = a^3$, and the cell averaged pressure is

$$\langle \zeta \rangle_s = \frac{4}{3\phi} \left(1 + \frac{\phi}{2} \right) (1 - \phi) \quad (\text{A7})$$

Therefore,

$$\zeta_{\text{eff.}} = \mu_s \langle \zeta \rangle_s - \frac{2}{3} \mu_s (1 - \phi) = \frac{4\mu_s}{3\phi} (1 - \phi) \quad (\text{A8})$$

(A8) uses definition (10), but the ζ 's in each solve different problems. (A8) is specific to the geometry of a sphere with cavity, while (10) is for a generic geometry occupying some fraction of the unit cube.

(A7) is plotted along with data for the numerical solutions of the cell problem posed on Y_s^{cube} in Figure 16. There is good agreement between (A7) and these computations for porosity $\gtrsim 10\%$ suggesting our deformation $Y_s^{\text{cube}} \Rightarrow Y_s^{\text{sphere}}$ was reasonable. We reiterate that though our result is quite similar to that of (11a) and (11b), the origin of the underlying Stokes problem is quite different.

Appendix B: Computational Methods and Results

B1. Cell Problem Boundary Conditions

Though we could solve the cell problems as stated, with the specified boundary conditions on interface γ and periodic on the rest of the domain, we use the symmetry of our model problems to reduce the computational cost by a factor of eight. The symmetry properties of the solutions allow us to formulate the appropriate boundary conditions on the portion of the boundary that is not γ . The symmetry properties of the cell problems are summarized in Table 5. We specify these Dirichlet boundary conditions on the velocity together with the original boundary condition on γ . When forming the weak form of the problem, we use neutral boundary conditions, $\sigma \cdot \mathbf{n} = 0$ on the part of the boundary

that is not γ . For example, in solving the permeability cell problem of Section 3.1 for \mathbf{k}^1 and q_1 , the weak form is

$$\int_{Y_f} \nabla \mathbf{k}^1 : \nabla \bar{\phi} - q_1 \nabla \cdot \bar{\phi} - \psi \nabla \cdot \mathbf{k}^1 = \int_{Y_f} \bar{\phi} \cdot \mathbf{e}_1 \quad (\text{B1})$$

where $\bar{\phi}$ and ψ are test functions. The Dirichlet boundary conditions are indicated in Figure 17. On the part of the boundary that is the interface, γ , we have applied the no-slip condition.

B2. Solver Algorithms

We discretize the Stokes equations for the cell problems using the P2-P1 formulation described in *Elman et al.* [2005]. The FEniCS libraries are used to generate code for the weak forms of the equations and assemble the associated matrices and vectors, [*Dupont et al.*, 2003; *Kirby and Logg*, 2006, 2007; *Logg*, 2007]. These vectors and matrices are passed to PETSc and solved using algebraic Multigrid preconditioned GMRES, [*Balay et al.*, 1997, 2004, 2001]. Domains and meshes were created with CUBIT [*Sandia Corporation*, 2008]. The versions of the software we used are summarized in Table 6.

To study problems with $O(10,000 - 100,000)$ elements and $O(100,000 - 1,000,000)$ unknowns, we rely on a Stokes preconditioner employing the pressure mass matrix of *Elman et al.* [2005]. The Stokes system is

$$\begin{pmatrix} \mathbf{A} & \mathbf{B}^T \\ \mathbf{B} & \mathbf{0} \end{pmatrix} \begin{bmatrix} \mathbf{u} \\ \mathbf{p} \end{bmatrix} = \mathbf{K} \begin{bmatrix} \mathbf{u} \\ \mathbf{p} \end{bmatrix} = \begin{bmatrix} \mathbf{f} \\ \mathbf{g} \end{bmatrix}$$

where \mathbf{A} is matrix corresponding to the weak form of the vector Laplacian, \mathbf{B}^T is the matrix corresponding to the weak form of the gradient, and \mathbf{B} is the matrix corresponding to the weak form of the divergence. This is preconditioned with an approximate inverse

of

$$\mathbf{P} = \begin{pmatrix} \mathbf{A} & \mathbf{0} \\ \mathbf{0} & \mathbf{Q} \end{pmatrix}$$

³⁶¹ \mathbf{Q} is the pressure-mass matrix.

³⁶² As our meshes are unstructured, the HYPRE library is used for algebraic multigrid
³⁶³ preconditioning. In particular, we use BoomerAMG. We apply this on all of \mathbf{P} , although
³⁶⁴ we could have only used this on the \mathbf{A} block, and relied on Jacobi or another light weight
³⁶⁵ pre-conditioner for the \mathbf{Q} block.

B3. Examples and Benchmarks

³⁶⁶ As a test, we solve the permeability cell problem of Section 3.1, with the symmetry
³⁶⁷ reductions, for flow past a sphere of radius 0.3. It is meshed with a characteristic size of
³⁶⁸ .03125, consisting of 119317 tetrahedrons. The results are summarized in Table 7

³⁶⁹ For comparison, *Jung and Torquato* [2005] ran a time dependent problem to steady
³⁷⁰ state and used an immersed boundary method with finite volumes. In our COMSOL
³⁷¹ computation, we used “fine” meshing, with 29649 elements, 134260 degrees of freedom,
³⁷² and a relative tolerance of 1e-10 in the solver.

³⁷³ The objective function, $\langle \mathbf{k}_1^1 \rangle$, converges as we refine our mesh; see Table 8 for a com-
³⁷⁴ parison of different meshes for this problem.

³⁷⁵ Table 9 summarizes the convergence results for flow around a sphere of radius 0.45.
³⁷⁶ Again, our method appears to be quite effective.

³⁷⁷ As another example, we solve the dilation stress cell problem from Section 3.2 . Solved
³⁷⁸ on the domain complementary to a spherical inclusion of radius 0.2, the convergence
³⁷⁹ results are summarized in Table 10.

380 The data in Tables 8– 10 were computed with default PETSc KSP tolerances. The
381 automatically generated mesh was constructed with the CUBIT command:

```
382 volume 6 sizing function type skeleton scale 3 time_accuracy_level 2  
383 min_size auto max_size 0.2 max_gradient 1.3
```

384 While these convergence results are encouraging, our data is imperfect. Continuing
385 with the dilation stress example, consider the data in Figure 18. Comparing Figures (a),
386 (c), and (e), it would appear that the domains with smaller fluid inclusions have less
387 well resolved pressure fields. They could likely be resolved with additional resolution.
388 However, we use this data and believe it to be valid for several reasons:

- 389 1. It is preferable to have all domains meshed with the same algorithm.
- 390 2. While the pressure fields may not be resolved, the error appears at the interface,
391 and we are interested in the cell average. Moreover, the relative variations about the cell
392 average are small.
- 393 3. The corresponding velocity fields, with magnitudes pictured in Figures (b), (d), and
394 (f), appear to be smooth, suggesting we are converging towards the analytical solution.
- 395 4. The cell averages are consistent with the trends from the better resolved cases.

B4. Cell Problem Data

396 All meshes were generated using CUBIT with the command:

```
397 volume 6 sizing function type skeleton scale 3 time_accuracy_level 2  
398 min_size auto max_size 0.2 max_gradient 1.3
```

399 Problems were solved in PETSc with a relative tolerance of 10^{-8} and and absolute
400 tolerance of 10^{-50} .

401 **Acknowledgments.** Both this paper and *Simpson et al.* [2008a] are based on the thesis
402 of G. Simpson, *Simpson* [2008], completed in partial fulfillment of the requirements for
403 the degree of doctor of philosophy at Columbia University.

404 The authors wish to thank D. Bercovici and R. Kohn for their helpful comments.

405 This work was funded in part by the US National Science Foundation (NSF) Collabo-
406 ration in Mathematical Geosciences (CMG), Division of Mathematical Sciences (DMS),
407 Grant DMS-05-30853, the NSF Integrative Graduate Education and Research Trainee-
408 ship (IGERT) Grant DGE-02-21041, NSF Grants DMS-04-12305 and DMS-07-07850.

References

409 Aharonov, E., M. Spiegelman, and P. Kelemen, Three-dimensional flow and reaction in
410 porous media: Implications for the Earth's mantle and sedimentary basins, *Journal of*
411 *Geophysical Research*, 102(7), 14,821–14,834, 1997.

412 Arzt, E., M. Ashby, and K. Easterling, Practical Applications of Hot Isostatic Pressing
413 Diagrams: Four Case Studies, *Metall. Trans A*, 14(2), 211–221, 1983.

414 Balay, S., W. D. Gropp, L. C. McInnes, and B. F. Smith, Efficient management of par-
415 allelism in object oriented numerical software libraries, in *Modern Software Tools in*
416 *Scientific Computing*, edited by E. Arge, A. M. Bruaset, and H. P. Langtangen, pp.
417 163–202, Birkhäuser Press, 1997.

418 Balay, S., K. Buschelman, W. D. Gropp, D. Kaushik, M. G. Knepley, L. C. McInnes,
419 B. F. Smith, and H. Zhang, PETSc Web page, <http://www.mcs.anl.gov/petsc>, 2001.

420 Balay, S., K. Buschelman, V. Eijkhout, W. D. Gropp, D. Kaushik, M. G. Knepley, L. C.
421 McInnes, B. F. Smith, and H. Zhang, PETSc users manual, *Tech. Rep. ANL-95/11 -*

- 422 *Revision 2.1.5*, Argonne National Laboratory, 2004.
- 423 Bear, J., *Dynamics of Fluids in Porous Media*, Courier Dover Publications, 1988.
- 424 Bercovici, D., Mantle dynamics past, present, and future: An introduction and overview,
425 in *Treatise on Geophysics*, vol. 7, edited by G. Schubert, Elsevier, 2007.
- 426 Bercovici, D., and Y. Ricard, Energetics of a two-phase model of lithospheric damage,
427 shear localization and plate-boundary formation, *Geophysical Journal International*,
428 *152*(3), 581–596, 2003.
- 429 Bercovici, D., and Y. Ricard, Tectonic plate generation and two-phase damage: Void
430 growth versus grain size reduction, *Journal of Geophysical Research*, *110*(B3), 2005.
- 431 Bercovici, D., Y. Ricard, and G. Schubert, A two-phase model for compaction and damage,
432 1: General theory, *Journal of Geophysical Research*, *106*(B5), 8887–8906, 2001.
- 433 Cheadle, M., Properties of texturally equilibrated two-phase aggregates, Ph.D. thesis,
434 University of Cambridge, 1989.
- 435 Cheadle, M., M. Elliott, and D. McKenzie, Percolation threshold and permeability of
436 crystallizing igneous rocks: The importance of textural equilibrium, *Geology*, *32*(9),
437 757–760, 2004.
- 438 Connolly, J., and Y. Podladchikov, Compaction driven fluid flow in viscoelastic rock,
439 *Geodinamica Acta-Revue de Geologie Dynamique et de Geographie Physique*, *11*(2),
440 55–84, 1998.
- 441 Doyen, P., Permeability, conductivity, and pore geometry of sandstone, *Journal of Geo-*
442 *physical Research*, *93*(B7), 7729–7740, 1988.
- 443 Dullien, F., *Porous Media: Fluid Transport and Pore Structure*, second edition ed., Aca-
444 demic Press, 1992.

445 Dupont, T., J. Hoffman, C. Johnson, R. C. Kirby, M. G. Larson, A. Logg, and L. R. Scott,
446 The FEniCS project, *Tech. Rep. 2003–21*, Chalmers Finite Element Center Preprint
447 Series, 2003.

448 Elman, H., D. Silvester, and A. Wathen, *Finite Elements and Fast Iterative Solvers: With*
449 *Applications in Incompressible Fluid Dynamics*, Oxford University Press, USA, 2005.

450 Faul, U., Permeability of partially molten upper mantle rocks from experiments and per-
451 colation theory, *J. Geophys. Res.*, *102*, 10,299–10,311, 1997.

452 Faul, U., Constraints on the melt distribution in anisotropic polycrystalline aggregates
453 undergoing grain growth, in *Physics and Chemistry of Partially Molten Rocks*, edited
454 by N. Bagdassarov, D. Laporte, and A. Thompson, pp. 141–178, Kluwer Academic,
455 2000.

456 Faul, U., D. Toomey, and H. Waff, Intergranular basaltic melt is distributed in thin,
457 elongated inclusions, *Geophysical Research Letters*, *21*(1), 29–32, 1994.

458 Hier-Majumder, S., Y. Ricard, and D. Bercovici, Role of grain boundaries in magma
459 migration and storage, *Earth and Planetary Science Letters*, *248*(3-4), 735–749, 2006.

460 Hirth, G., and D. Kohlstedt, Experimental constraints on the dynamics of the partially
461 molten upper mantle: Deformation in the diffusion creep regime, *Journal of Geophysical*
462 *Research*, *100*(B2), 1981–2001, 1995a.

463 Hirth, G., and D. Kohlstedt, Experimental constraints on the dynamics of the partially
464 molten upper mantle 2: Deformation in the dislocation creep regime, *Journal of Geo-*
465 *physical Research*, *100*(B2), 15,441–15,449, 1995b.

466 Jung, Y., and S. Torquato, Fluid permeabilities of triply periodic minimal surfaces, *Phys-*
467 *ical Review E*, *72*(5), 56,319, 2005.

- 468 Katz, R., M. Spiegelman, and S. Carbotte, Ridge migration, asthenospheric flow and the
469 origin of magmatic segmentation in the global mid-ocean ridge system, *Geophys. Res.*
470 *Letts*, 31, 2004.
- 471 Katz, R., M. Spiegelman, and B. Holtzman, The dynamics of melt and shear localization
472 in partially molten aggregates., *Nature*, 442(7103), 676–9, 2006.
- 473 Kelemen, P., G. Hirth, N. Shimizu, M. Spiegelman, and H. Dick, A review of melt migra-
474 tion processes in the adiabatically upwelling mantle beneath oceanic spreading ridges,
475 *Philosophical Transactions of the Royal Society A: Mathematical, Physical and Engi-*
476 *neering Sciences*, 355(1723), 283–318, 1997.
- 477 Kirby, R. C., and A. Logg, A compiler for variational forms, *ACM Transactions on Math-*
478 *ematical Software*, 32(3), 417–444, 2006.
- 479 Kirby, R. C., and A. Logg, Efficient compilation of a class of variational forms, *ACM*
480 *Transactions on Mathematical Software*, 33(3), 2007.
- 481 Kohlstedt, D., Properties of rocks and minerals – constitutive equations, rheological be-
482 havior, and viscosity of rocks, in *Treatise on Geophysics*, vol. 2, edited by G. Schubert,
483 Elsevier, 2007.
- 484 Kohlstedt, D., Q. Bai, Z. Wang, and S. Mei, Rheology of partially molten rocks, in *Physics*
485 *and Chemistry of Partially Molten Rocks*, edited by N. Bagdassarov, D. Laporte, and
486 A. Thompson, pp. 3–28, Kluwer Academic, 2000.
- 487 Koponen, A., M. Kataja, and J. Timonen, Permeability and effective porosity of porous
488 media, *Physical Review E*, 56(3), 3319–3325, 1997.
- 489 Logg, A., Automating the finite element method, *Arch. Comput. Methods Eng.*, 14(2),
490 93–138, 2007.

- 491 Martys, N., S. Torquato, and D. Bentz, Universal scaling of fluid permeability for sphere
492 packings, *Physical Review E*, 50(1), 403–408, 1994.
- 493 McKenzie, D., The generation and compaction of partially molten rock, *Journal of Petrol-*
494 *ogy*, 25(3), 713–765, 1984.
- 495 Nye, J., The flow law of ice from measurements in glacier tunnels, laboratory experiments
496 and the Jungfraufirn borehole experiment, *Proceedings of the Royal Society of London.*
497 *Series A, Mathematical and Physical Sciences*, pp. 477–489, 1953.
- 498 Prud’homme, R., and R. Bird, The dilational properties of suspensions of gas bubbles in
499 incompressible newtonian and non-newtonian fluids, *Journal of Non-Newtonian Fluid*
500 *Mechanics*, 3(3), 261–279, 1978.
- 501 Ricard, Y., Physics of mantle convection, in *Treatise on Geophysics*, vol. 7, edited by
502 G. Schubert, Elsevier, 2007.
- 503 Ricard, Y., D. Bercovici, and G. Schubert, A two-phase model of compaction and damage,
504 2: Applications to compaction, deformation, and the role of interfacial surface tension,
505 *Journal of Geophysical Research*, 106, 8907–8924, 2001.
- 506 Richter, F., and D. McKenzie, Dynamical models for melt segregation from a deformable
507 matrix, *Journal of Geology*, 92(6), 729–740, 1984.
- 508 Sandia Corporation, CUBIT, <http://cubit.sandia.gov/>, 2008.
- 509 Scheidegger, A., *The physics of flow through porous media: Third edition*, University of
510 Toronto Press, 1974.
- 511 Schmeling, H., Partial melting and melt segregation in a convecting mantle, in *Physics*
512 *and Chemistry of Partially Molten Rocks*, edited by N. Bagdassarov, D. Laporte, and
513 A. Thompson, pp. 141–178, Kluwer Academic, 2000.

- 514 Scott, D., and D. Stevenson, Magma solitons, *Geophysical Research Letters*, 11(11), 1161–
515 1161, 1984.
- 516 Simpson, G., The mathematics of magma migration, Ph.D. thesis, Columbia University,
517 2008.
- 518 Simpson, G., and M. Weinstein, Asymptotic stability of ascending solitary magma waves,
519 *SIAM J. Math. Anal.*, 40, 1337–1391, 2008.
- 520 Simpson, G., M. Spiegelman, and M. Weinstein, Degenerate dispersive equations arising
521 in the study of magma dynamics, *Nonlinearity*, 20, 21–49, 2007.
- 522 Simpson, G., M. Spiegelman, and M. Weinstein, A multiscale model of partial melts 1:
523 Effective equations, submitted to *Journal of Geophysical Research*, 2008a.
- 524 Simpson, G., M. Spiegelman, and M. Weinstein, A multiscale model of partial melts 2:
525 Numerical results, submitted to *Journal of Geophysical Research*, 2008b.
- 526 Simpson, G., M. Weinstein, and P. Rosenau, On a hamiltonian pde arising in magma
527 dynamics, *DCDS-B*, 10, 903–924, 2008c.
- 528 Spiegelman, M., Flow in deformable porous media. part 1: Simple analysis, *Journal of*
529 *Fluid Mechanics*, 247, 17–38, 1993a.
- 530 Spiegelman, M., Flow in deformable porous media. part 2: Numerical analysis, *Journal*
531 *of Fluid Mechanics*, 247, 39–63, 1993b.
- 532 Spiegelman, M., Physics of Melt Extraction: Theory, Implications and Applications,
533 *Philosophical Transactions: Physical Sciences and Engineering*, 342(1663), 23–41,
534 1993c.
- 535 Spiegelman, M., Geochemical consequences of melt transport in 2-D: The sensitivity of
536 trace elements to mantle dynamics, *Earth and Planetary Science Letters*, 139(1-2),

- 537 115–132, 1996.
- 538 Spiegelman, M., Linear analysis of melt band formation by simple shear, *Geochemistry,*
539 *Geophysics, Geosystems*, 4(9), 8615, 2003.
- 540 Spiegelman, M., and P. Kelemen, Extreme chemical variability as a consequence of chan-
541 nelized melt transport, *Geochemistry, Geophysics, Geosystems*, 4(7), 1055, 2003.
- 542 Spiegelman, M., and D. McKenzie, Simple 2-D models for melt extraction at mid-ocean
543 ridges and island arcs, *Earth and Planetary Science Letters*, 83(1-4), 137–152, 1987.
- 544 Spiegelman, M., P. Kelemen, and E. Aharonov, Causes and consequences of flow organi-
545 zation during melt transport: The reaction infiltration instability in compactible media,
546 *Journal of Geophysical Research*, 106(B2), 2061–2077, 2001.
- 547 Spiegelman, M., R. Katz, and G. Simpson, An Introduction and Tutorial to the
548 “McKenize Equations” for magma migration, [http://www.geodynamics.org/cig/
549 workinggroups/magma/workarea/benchmark/McKenzieIntroBenchmarks.pdf](http://www.geodynamics.org/cig/workinggroups/magma/workarea/benchmark/McKenzieIntroBenchmarks.pdf), 2007.
- 550 Stevenson, D., and D. Scott, Mechanics of Fluid-Rock Systems, *Annual Review of Fluid*
551 *Mechanics*, 23(1), 305–339, 1991.
- 552 Taylor, G., The two coefficients of viscosity for an incompressible fluid containing air bub-
553 bles, *Proceedings of the Royal Society of London. Series A, Mathematical and Physical*
554 *Sciences*, 226(1164), 34–37, 1954.
- 555 Torquato, S., *Random Heterogeneous Materials: Microstructure and Macroscopic Proper-*
556 *ties*, Springer, 2002.
- 557 Turcotte, D., and G. Schubert, *Geodynamics*, Second ed., Cambridge University Press,
558 2002.

- 559 Vasilyev, O., Y. Podladchikov, and D. Yuen, Modeling of compaction driven flow in poro-
560 viscoelastic medium using adaptive wavelet collocation method, *Geophysical Research*
561 *Letters*, *25*(17), 3239–3242, 1998.
- 562 von Bagen, N., and H. Waff, Permeabilities, interfacial areas and curvatures of partially
563 molten systems: Results of numerical computations of equilibrium microstructures,
564 *Journal of Geophysical Research*, *91*(B9), 9261–9276, 1986.
- 565 Wark, D., and E. Watson, Grain-scale permeabilities of texturally equilibrated, monomin-
566 eralic rocks, *Earth and Planetary Science Letters*, *164*(3-4), 591–605, 1998.
- 567 Wark, D., C. Williams, E. Watson, and J. Price, Reassessment of pore shapes in mi-
568 crostructurally equilibrated rocks, with implications for permeability of the upper man-
569 tle, *Journal of Geophysical Research*, *108*(2050), 2003.
- 570 Zhu, W., and G. Hirth, A network model for permeability in partially molten rocks, *Earth*
571 *and Planetary Science Letters*, *212*(3-4), 407–416, 2003.

Table 1. Notation for macroscopic equations derived by homogenization.

Symbol	Meaning
$\delta_{\text{comp.}}$	Compaction length
$e(\mathbf{v})$	Strain rate tensor, $e(\mathbf{v}) = \frac{1}{2}(\nabla\mathbf{v} + (\nabla\mathbf{v})^T)$
$\eta_{\text{eff.}}$	Supplementary anisotropic viscosity derived by homogenization
ϕ	Porosity
K	Permeability tensor of the matrix derived by homogenization
$k_{\text{eff.}}$	Isotropic permeability of the matrix derived by homogenization
μ_f	Shear viscosity of the melt
μ_s	Shear viscosity of the matrix
P	Macroscopic (fluid) pressure derived by homogenization
ρ_f	Melt density
ρ_s	Matrix density
$\bar{\rho}$	Mean density, $\bar{\rho} = \rho_f\phi + (1 - \phi)\rho_s$
\mathbf{V}^f	Macroscopic fluid velocity derived by homogenization
\mathbf{V}^s	Macroscopic solid velocity derived by homogenization
$\zeta_{\text{eff.}}$	Bulk viscosity of the matrix derived by homogenization

Table 2. Notation for constitutive relations in other models.

Symbol	Meaning
ϕ_*	Critical porosity for activation of μ_{s+f} viscosity
κ	Permeability of the matrix
μ_{s+f}	Shear viscosity of the matrix in the presence of melt
ζ_s	Bulk viscosity of the matrix

Table 3. Notation for cell problems.

Symbol	Meaning
ϵ	Ratio of microscopic and macroscopic length scales, $\epsilon = \ell/L$
$e_y(\mathbf{v})$	Strain rate tensor, $e_y(\mathbf{v}) = \frac{1}{2}(\nabla_y \mathbf{v} + (\nabla_y \mathbf{v})^T)$
γ	Interface between melt and matrix within cell Y
ℓ	Grain length scale
L	Macroscopic length scale
∇_y	Gradient taken with respect to the \mathbf{y} argument
$\nabla_y \cdot$	Divergence taken with respect to the \mathbf{y} argument
Ω	Macroscopic region containing both melt and matrix
\mathbf{y}	Coordinate within the cell, Y
Y	The unit cell
Y_f	Portion of unit cell occupied by melt
Y_s	Portion of unit cell occupied by matrix
ζ	Pressure of the cell problem for a unit forcing on the divergence equation

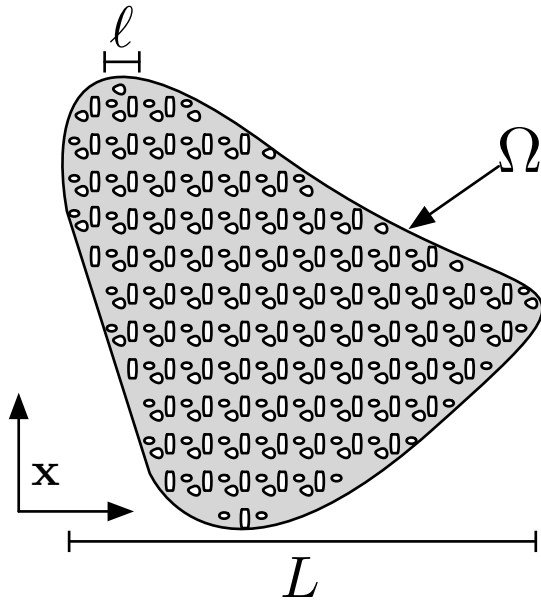


Figure 1. The macroscopic domain Ω . The gray body is occupied by the matrix and the white inclusions are the melt.

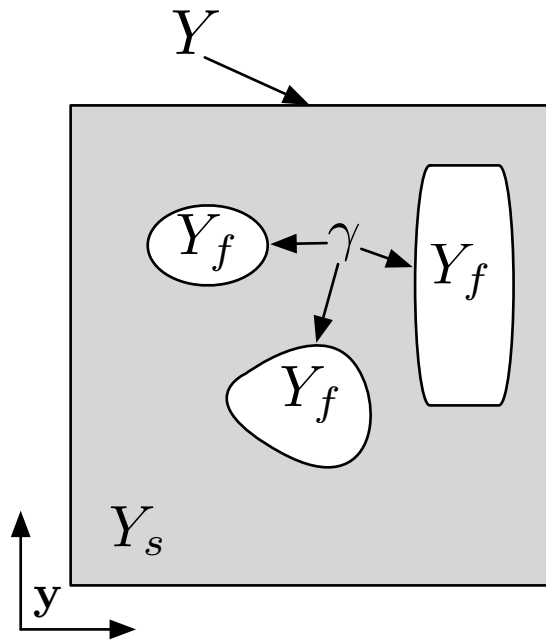
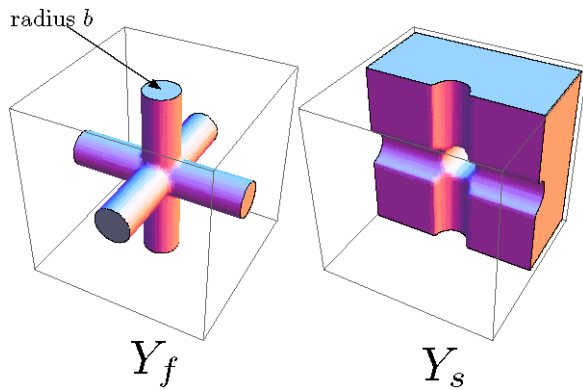


Figure 2. The cell domain, Y , divided into fluid and solid regions, Y_f and Y_s . The two phases meet on interface γ .

Table 4. Notation for cell problems, continued.

Symbol	Meaning
$\bar{\chi}^{lm}$	Velocity of the cell problem for a unit shear stress forcing on the solid in the lm component of the stress tensor
\mathbf{e}_i	Unit vector in the i -th coordinate, $\mathbf{e}_1^T = (1, 0, 0)$
ϕ_{eff}	Effective porosity, portion of the porosity in which there is appreciable flow. $\phi_{\text{eff}} \leq \phi$.
\mathbf{k}^i	Velocity of the cell problem for a unit forcing on the fluid in the \mathbf{e}_i direction
\mathbf{k}_1^1	First component of the velocity from the cell problem with unit forcing on the fluid in the \mathbf{e}_1 direction
$\bar{\xi}$	Velocity of the cell problem for a unit forcing on the divergence equation
$\langle \cdot \rangle_f$	Volume average of a quantity over the melt portion of a cell, $\langle \cdot \rangle_f = \int_{Y_f} \cdot d\mathbf{y}$
$\langle \cdot \rangle_s$	Volume average of a quantity over the matrix portion of a cell, $\langle \cdot \rangle_s = \int_{Y_s} \cdot d\mathbf{y}$
π^{lm}	Pressure of the cell problem for a unit shear stress forcing on the solid in the lm component of the the stress tensor
q^i	Pressure of the cell problem for a unit forcing on the fluid in the \mathbf{e}_i direction
ζ	Pressure of the cell problem for a unit forcing on the divergence equation

**Figure 3.** A cell geometry composed of triply intersecting cylinders of equal radius.

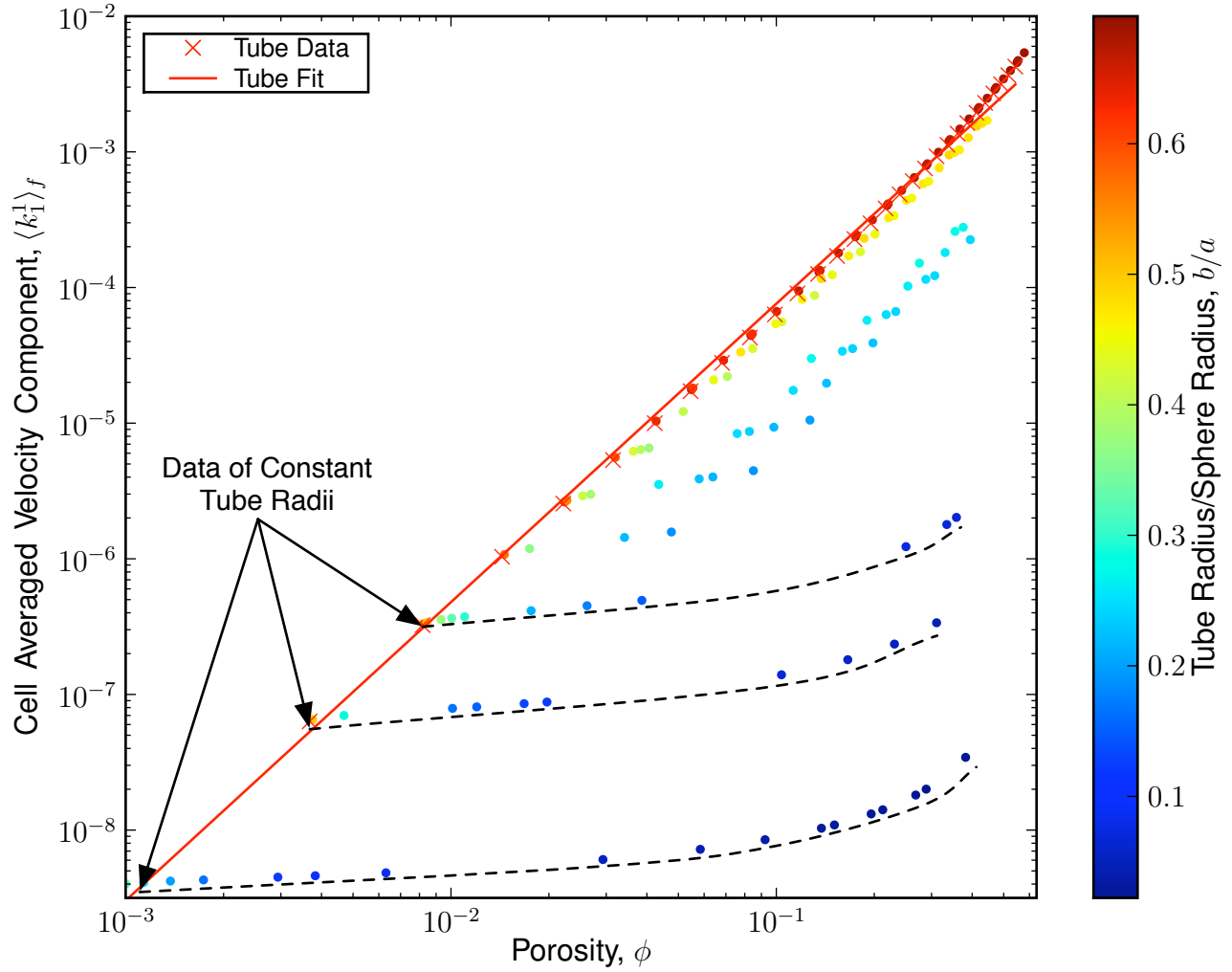


Figure 4. Numerically computed values of $\langle k_1^1 \rangle_f$, the effective permeability, plotted against porosity for both the tube geometry and the sphere+tube geometry. The scattered circles are data from sphere+tube geometries, colored by the ratio of tube radius to sphere radius. The tube geometry offers an upper bound for a given porosity.

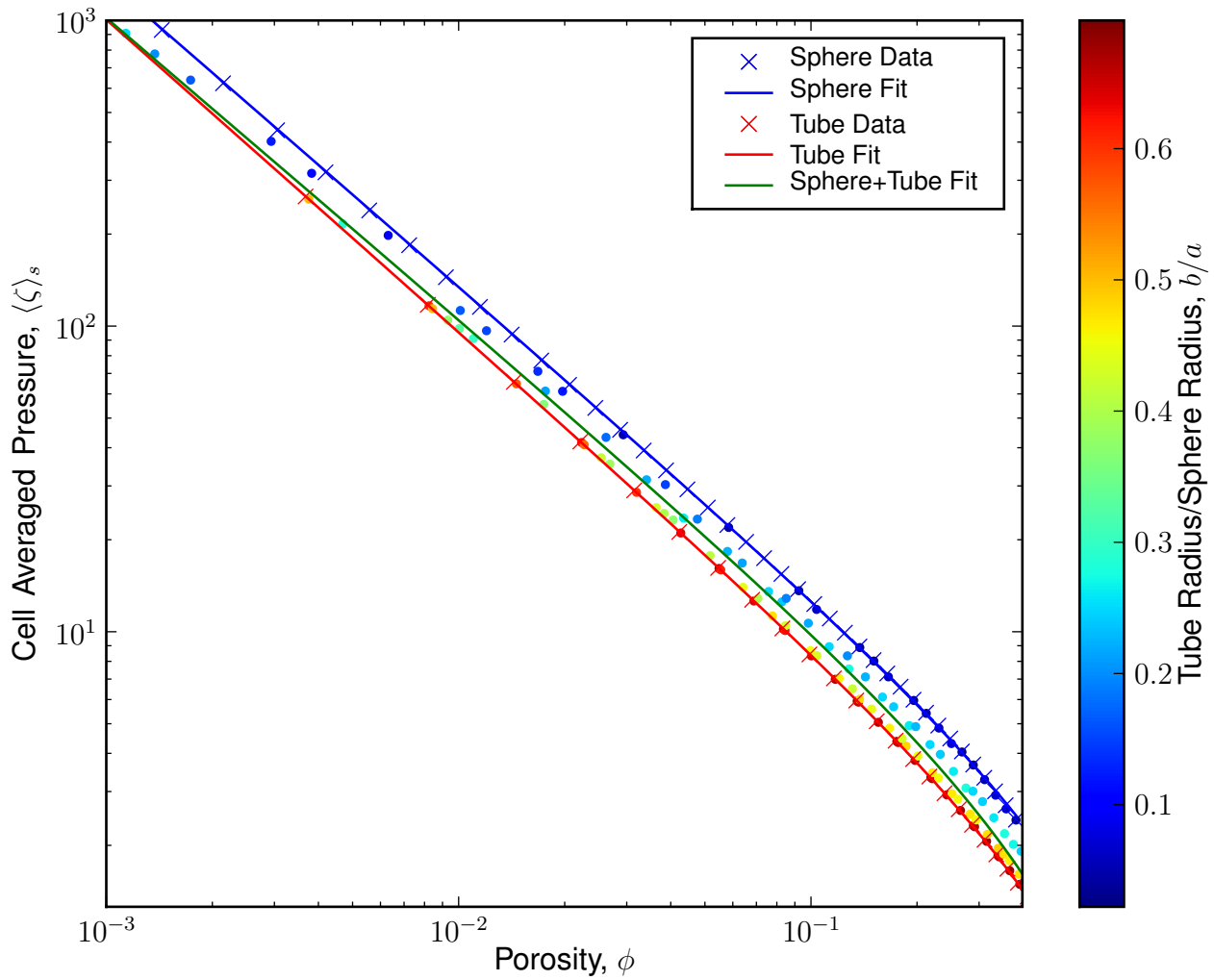


Figure 5. Numerically computed data for the dilation stress cell problem, (9a–9c), on the three geometries, along with the least square fits (12), (26a), and (26b)). The scattered circles are data from sphere+tube geometries, colored by the ratio of tube radius to sphere radius. The sphere+tube data is bounded between the the tube data and the sphere data.

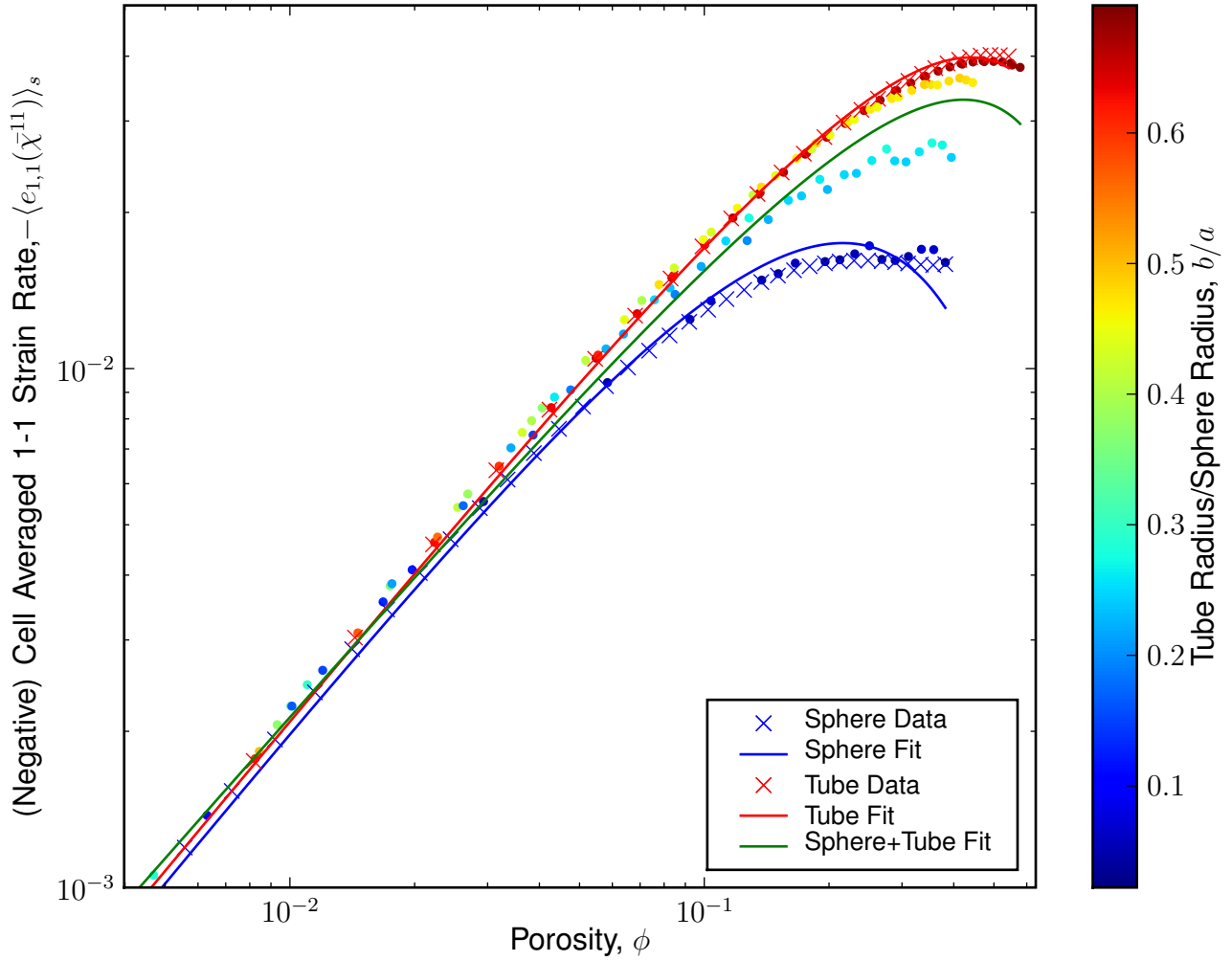


Figure 6. Numerically computed data for the normal stress cell problem on the three geometries, along with the least square fits (15), (27a), and (27b). The scattered circles are data from sphere+tube geometries, colored by the ratio of tube radius to sphere radius. At small porosity there is little variation amongst the simulated domains.

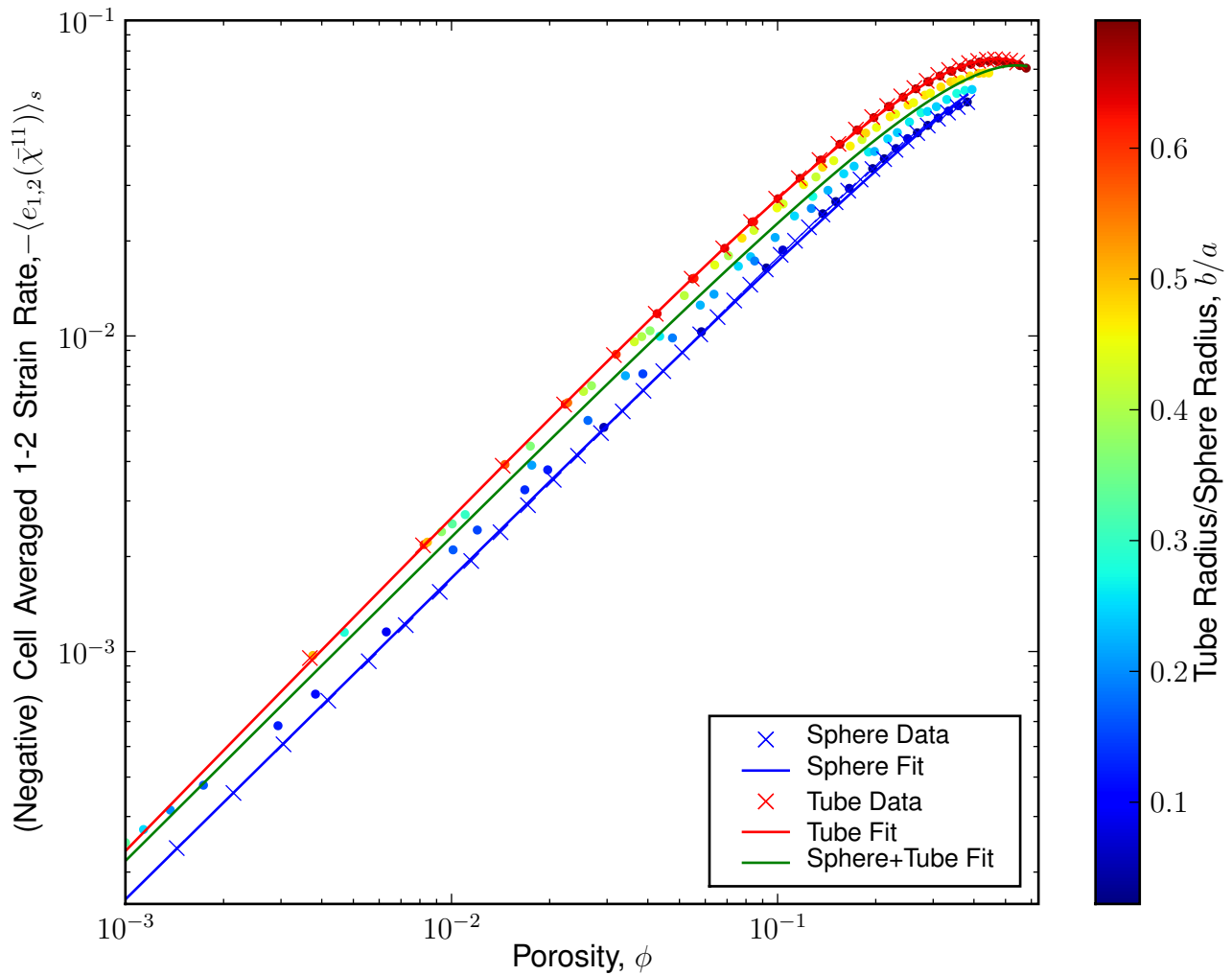


Figure 7. Numerically computed data for the shear stress cell problem on the three geometries, along with the least square fits (16), (28a), (28b). The scattered circles are data from sphere+tube geometries, colored by the ratio of tube radius to sphere radius. Sphere+Tube data points are constrained between the sphere data and the tube data. At all simulated porosities, there is less than an order of magnitude of variation.

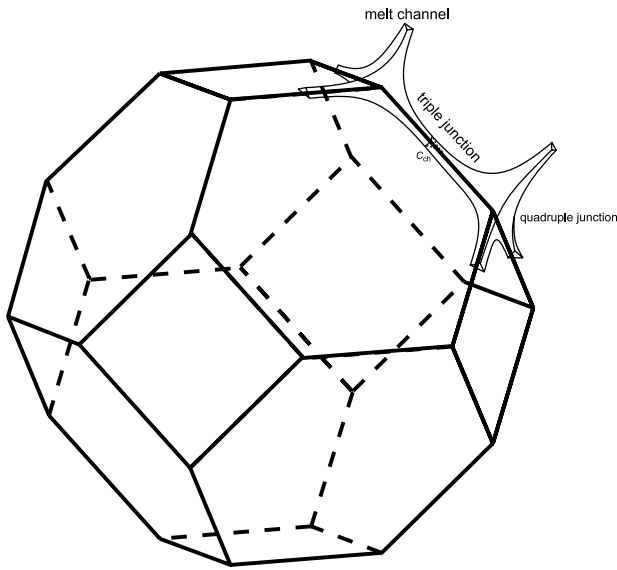


Figure 8. An idealized Olivine grain from Figure 1 of *Zhu and Hirth* [2003]. Melt channels are found at triple junctions, while melt pockets are found quadruple junctions.

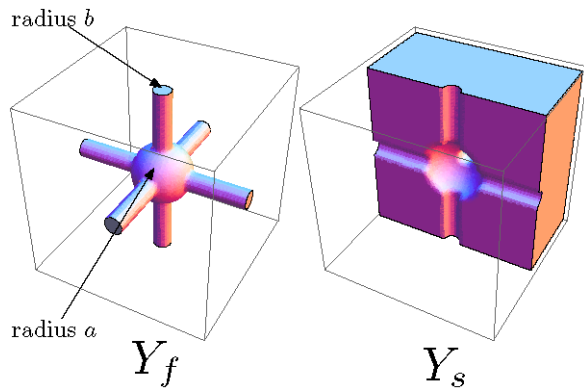


Figure 9. A cell geometry composed of triply intersecting cylinders of equal radius, with a sphere at the intersection.

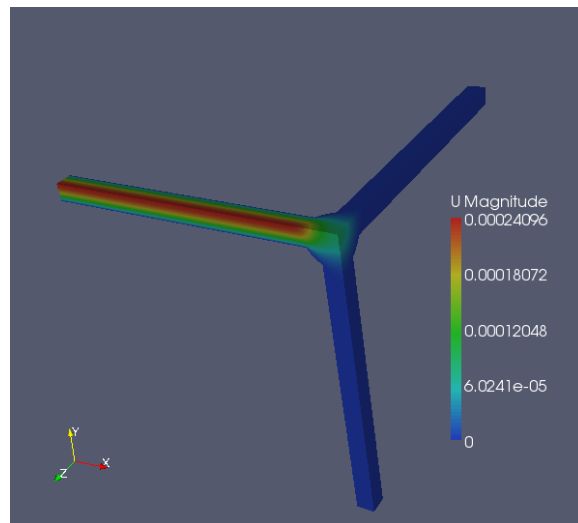


Figure 10. The magnitude of the velocity for a permeability cell problem. This corresponds to the sphere+tube domain with sphere radius $a = .06$ and tube radius $b = .03$.

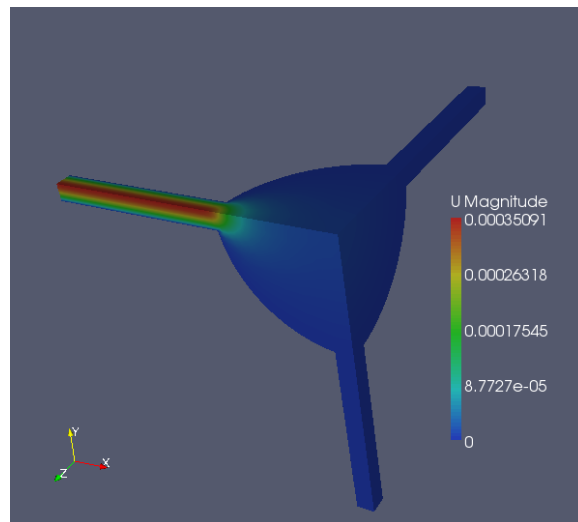


Figure 11. The magnitude of the velocity for a permeability cell problem. This corresponds to the sphere+tube domain with sphere radius $a = .20$ and tube radius $b = .03$.

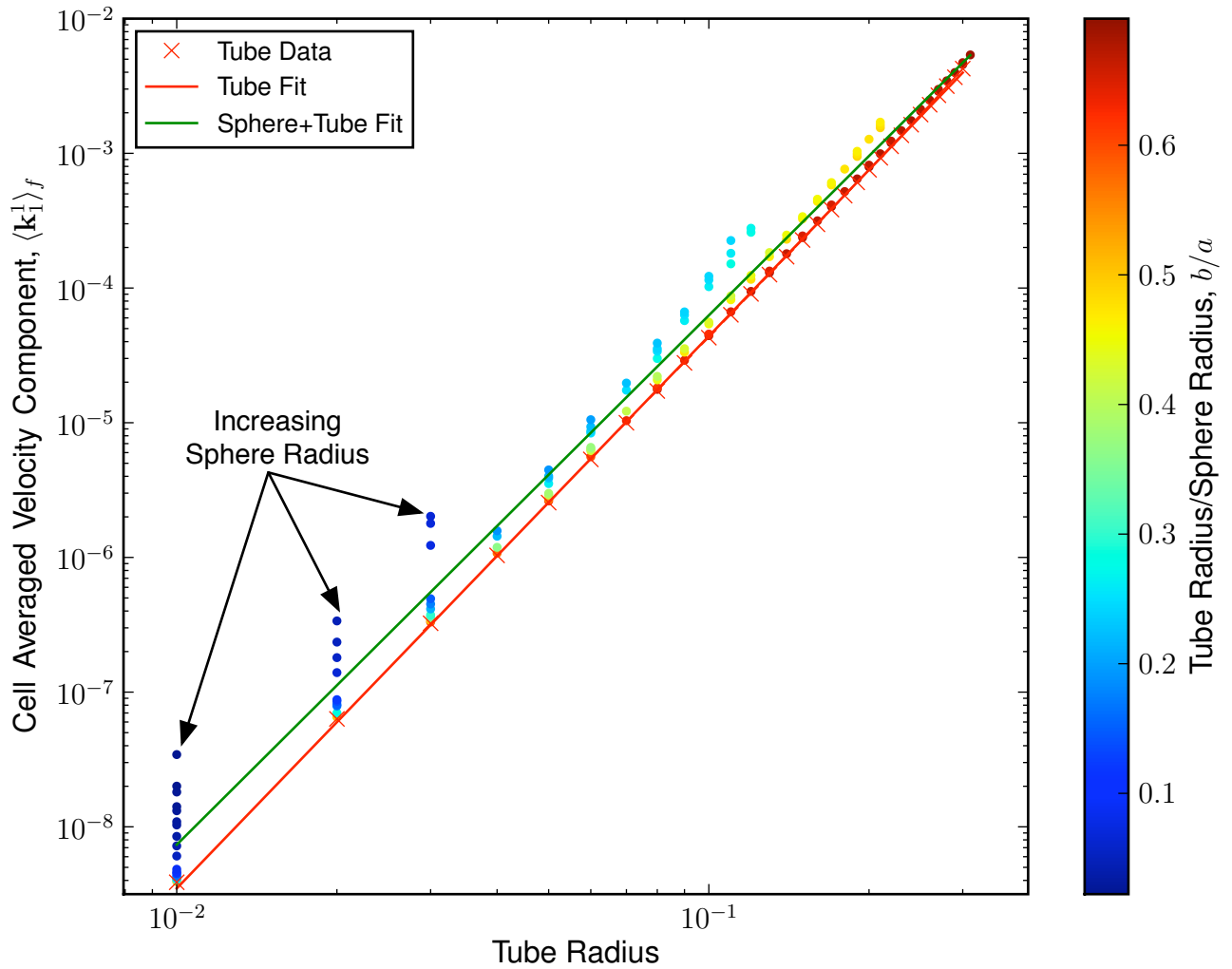


Figure 12. $\langle \mathbf{k}_1^1 \rangle_f$, the effective permeability, plotted against tube radius for both the tube geometry and the sphere+tube geometry. The scattered circles are data from sphere+tube geometries, colored by the ratio of tube radius to sphere radius. The tube geometry offers a lower bound for a given porosity.

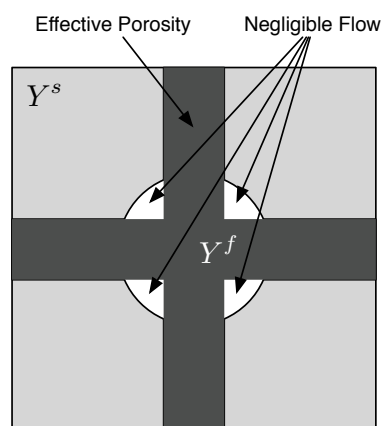


Figure 13. The dark portion is the postulated effective porosity for the sphere+tube domains.

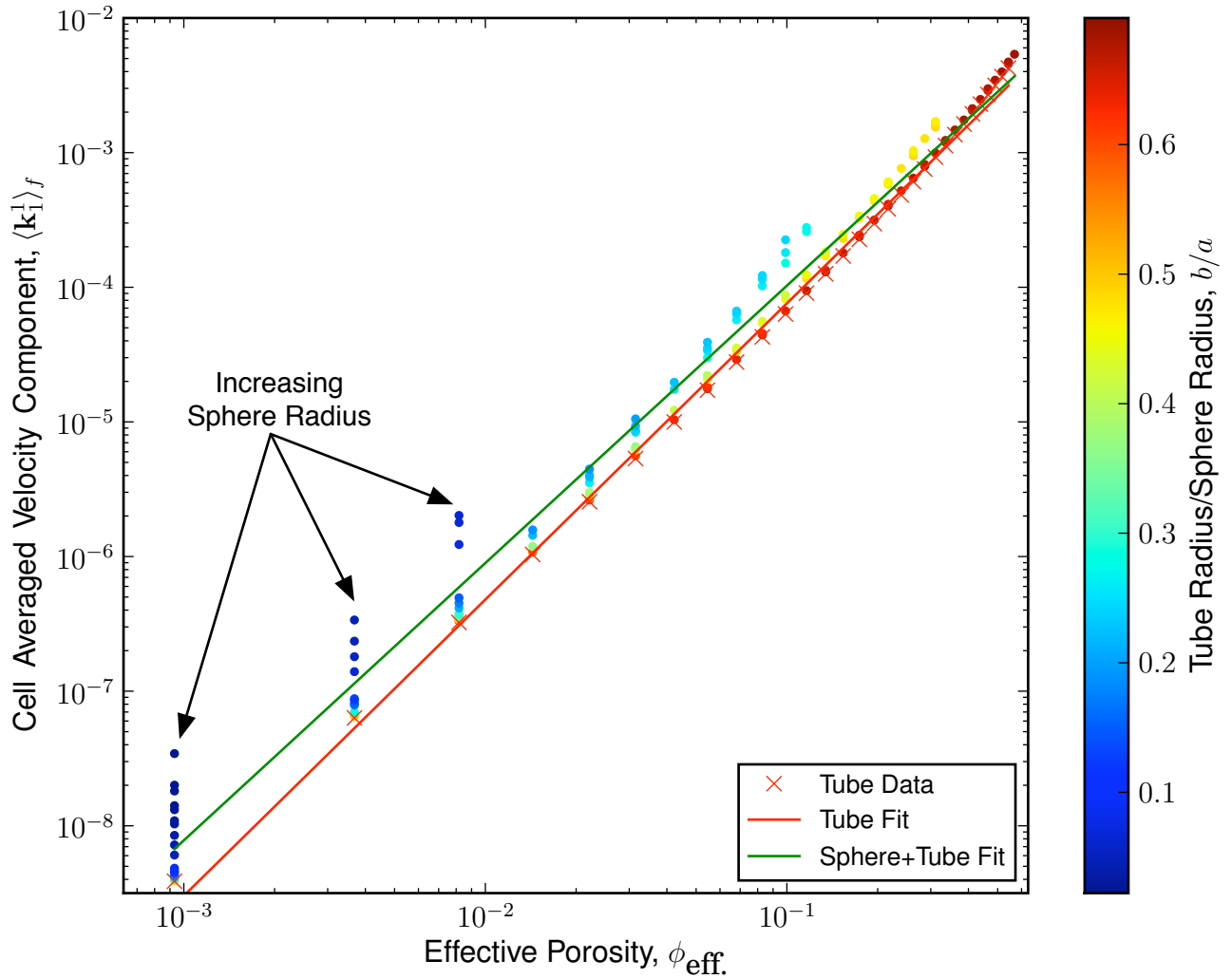


Figure 14. $\langle k_1^1 \rangle_f$, the permeability, plotted against the effective porosity for the sphere+tube geometry. The scattered circles are data from sphere+tube geometries, colored by the ratio of tube radius to sphere radius. The tube data plotted against porosity also appears.

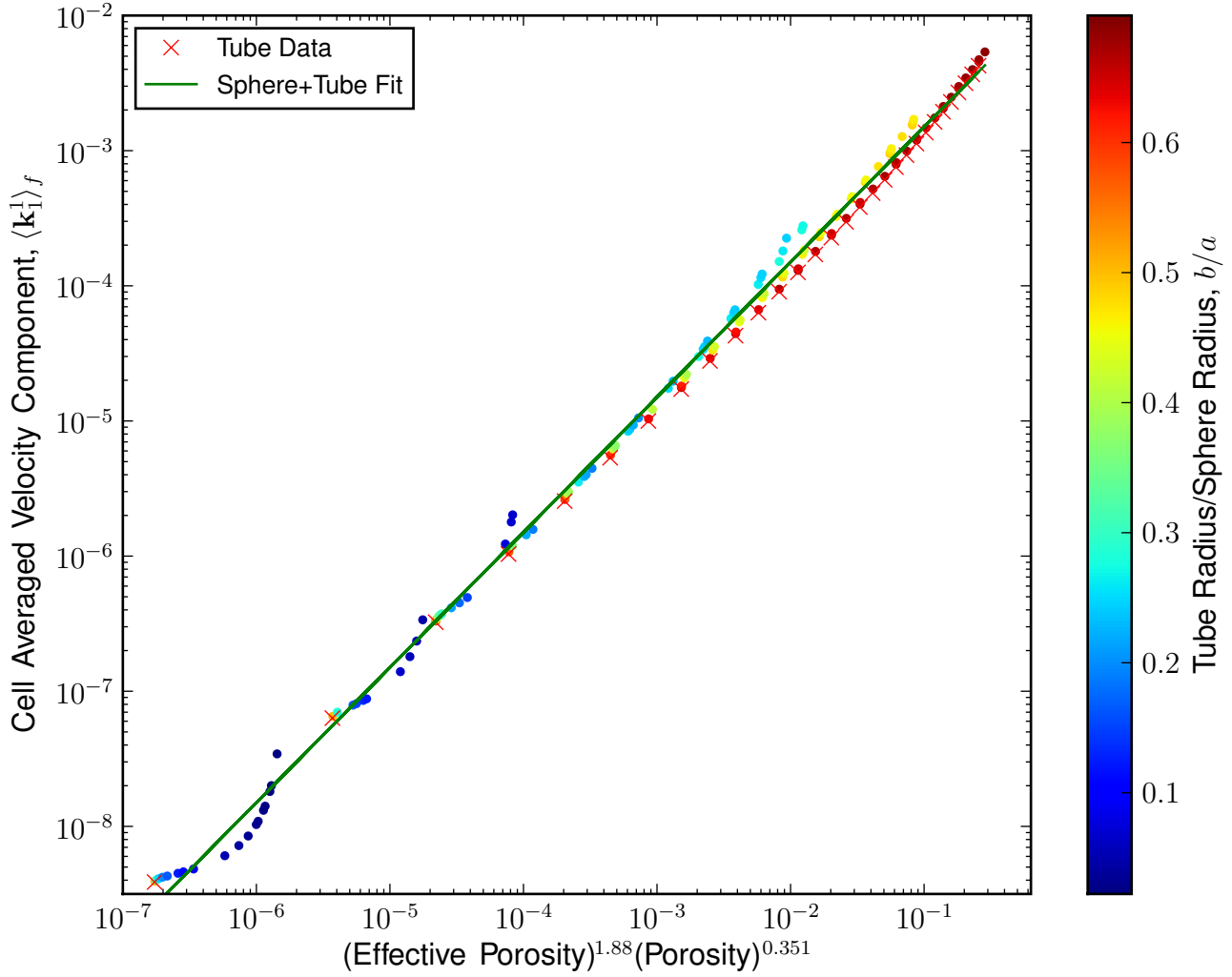


Figure 15. $\langle \mathbf{k}_1^1 \rangle_f$, the permeability, plotted against the effective porosity and porosity, using (23). The scattered circles are data from sphere+tube geometries, colored by the ratio of tube radius to sphere radius. The tube data is also plotted, substituting ϕ for ϕ_{eff} in (23).

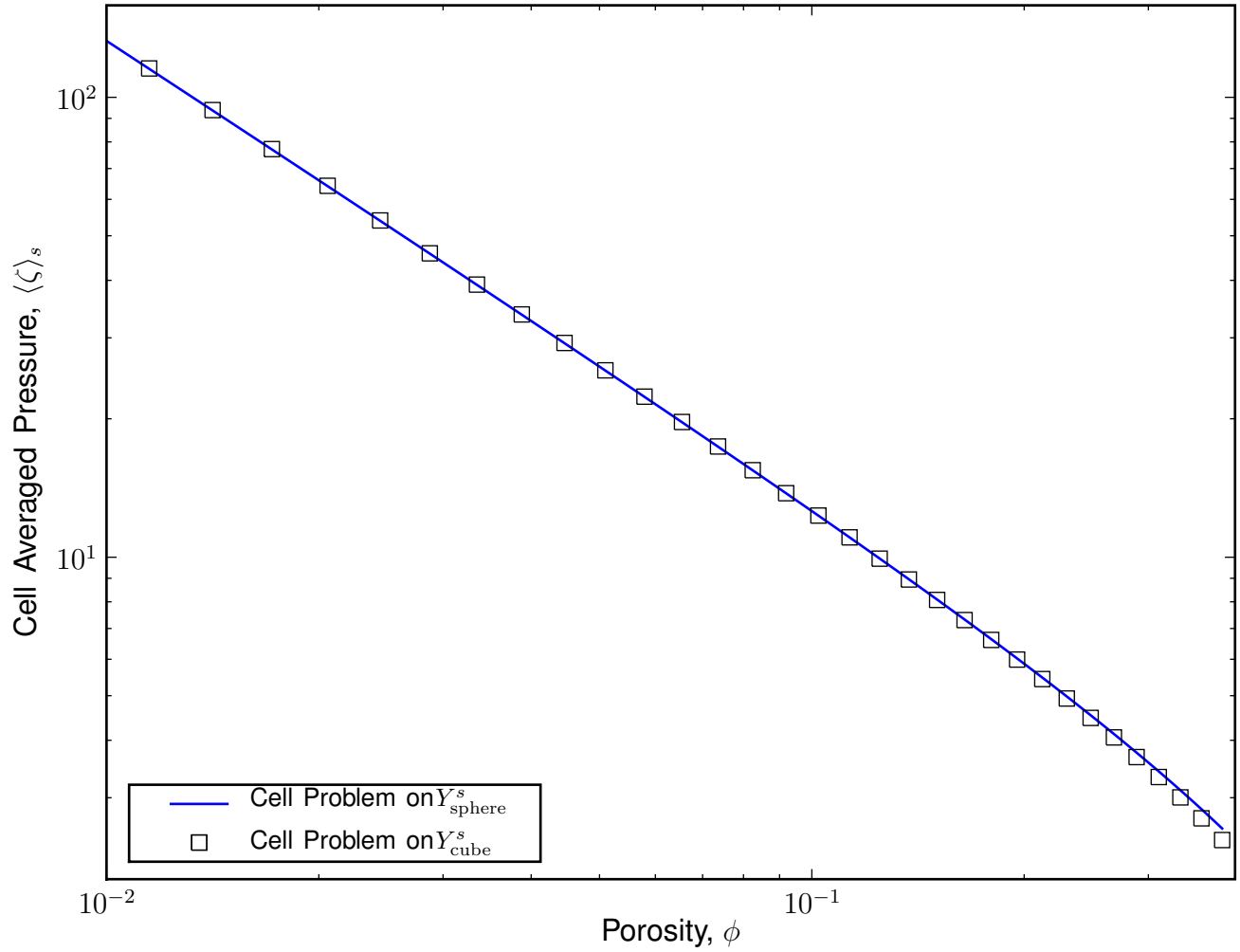


Figure 16. Cell averaged pressure, (A7), plotted as a function of porosity. The data from the numerical solution of the cell problem given by equations (9a – 9c) and posed on Y_s^{cube} also appears. It is in good agreement with the analytic solution on the spherical domain, Y_s^{sphere} .

Table 5. Summary of symmetry conditions used as Dirichlet boundary conditions in the cell problem computations.

Cell Problem Velocity	$y_1 = 0, -.5$	$y_2 = 0, -.5$	$y_3 = 0, -.5$
\mathbf{k}^1	$\mathbf{k}_2^1 = \mathbf{k}_3^1 = 0$	$\mathbf{k}_2^1 = 0$	$\mathbf{k}_3^1 = 0$
$\bar{\chi}^{11}$	$\bar{\chi}_1^{11} = 0$	$\bar{\chi}_2^{11} = 0$	$\bar{\chi}_3^{11} = 0$
$\bar{\chi}^{12}$	$\bar{\chi}_2^{12}, \bar{\chi}_3^{12} = 0$	$\bar{\chi}_1^{12} = \bar{\chi}_3^{12} = 0$	$\bar{\chi}_3^{12} = 0$
$\bar{\xi}$	$\bar{\xi}_1 = 0$	$\bar{\xi}_2 = 0$	$\bar{\xi}_3 = 0$

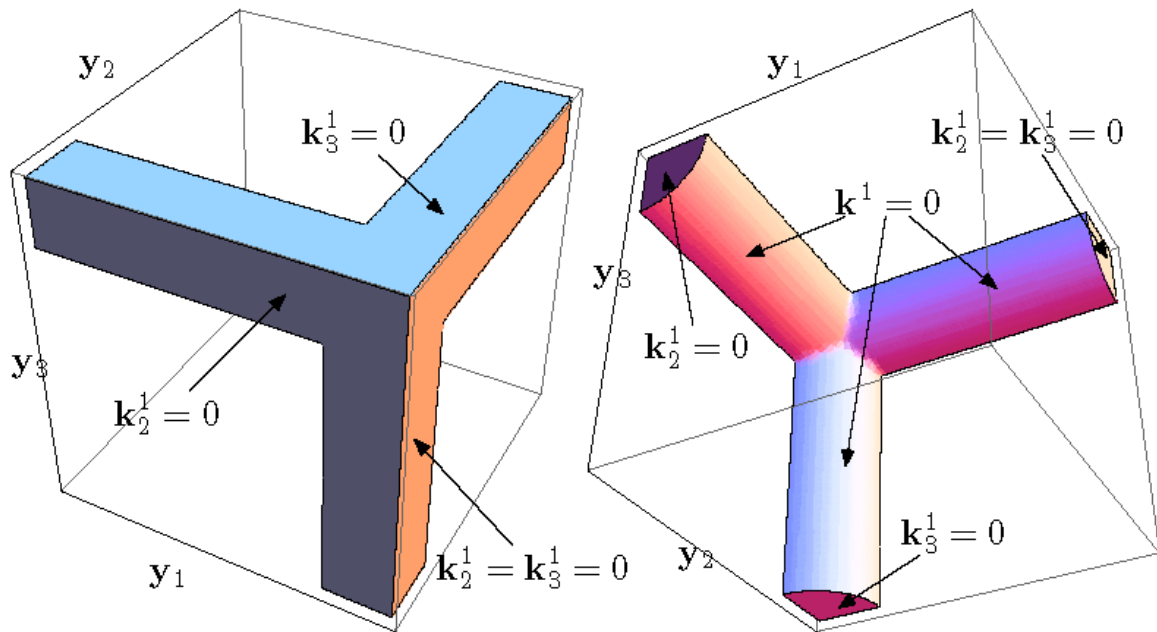


Figure 17. Specification of Dirichlet boundary conditions on \mathbf{k}^1 when solving on a symmetry reduced domain.

Table 6. Software versions

Package	Version
CUBIT	11.0
DOLFIN(FEniCS)	0.7.2
FFC(FEniCS)	0.4.4
FIAT(FEniCS)	0.3.4
HYPRE	2.0.0
PETSc	2.3.3
UFC(FEniCS)	1.1
UMFPACK	4.3

Table 7. Convergence comparison between solvers

Method	$\langle \mathbf{k}_1^1 \rangle$
BoomerAMG on \mathbf{P} + GMRES	0.0447051
JT05	0.045803
COMSOL	0.044497

Table 8. Convergence data for permeability cell problem I

Mesh Size	No. Cells	No. d.o.f.	$\langle \mathbf{k}_1^1 \rangle_f$	$ \% \Delta $
0.25	56	430	0.0492875	–
0.125	534	2950	0.0472207	0.0419336
0.0625	3673	17988	0.0452142	0.042492
0.03125	26147	119317	0.0447051	0.0112597
auto	14803	70525	0.0445419	–

Table 9. Convergence data for permeability cell problem II

Mesh Size	No. Cells	No. d.o.f.	$\langle \mathbf{k}_1^1 \rangle_f$	$ \% \Delta $
0.25	61	475	0.00763404	–
0.125	384	2302	0.00651896	0.146067
0.0625	2620	13370	0.00626809	0.0384831
0.03125	19916	93011	0.00617889	0.0142308
auto	23776	112620	0.00616139	–
JT05	–	–	0.0064803	–
COMSOL	–	–	0.006153	–

Table 10. Convergence data for dilation stress cell problem

Mesh Size	No. Cells	No. d.o.f.	$\langle \zeta \rangle_s$	$ \% \Delta $
0.25	73	541	46.6432	–
0.125	514	2862	44.1747	0.052923
0.0625	3813	18575	40.7177	0.0782575
0.03125	29063	132115	39.4805	0.0303848
auto	13725	64205	39.1558	–
COMSOL	–	–	39.117074	–

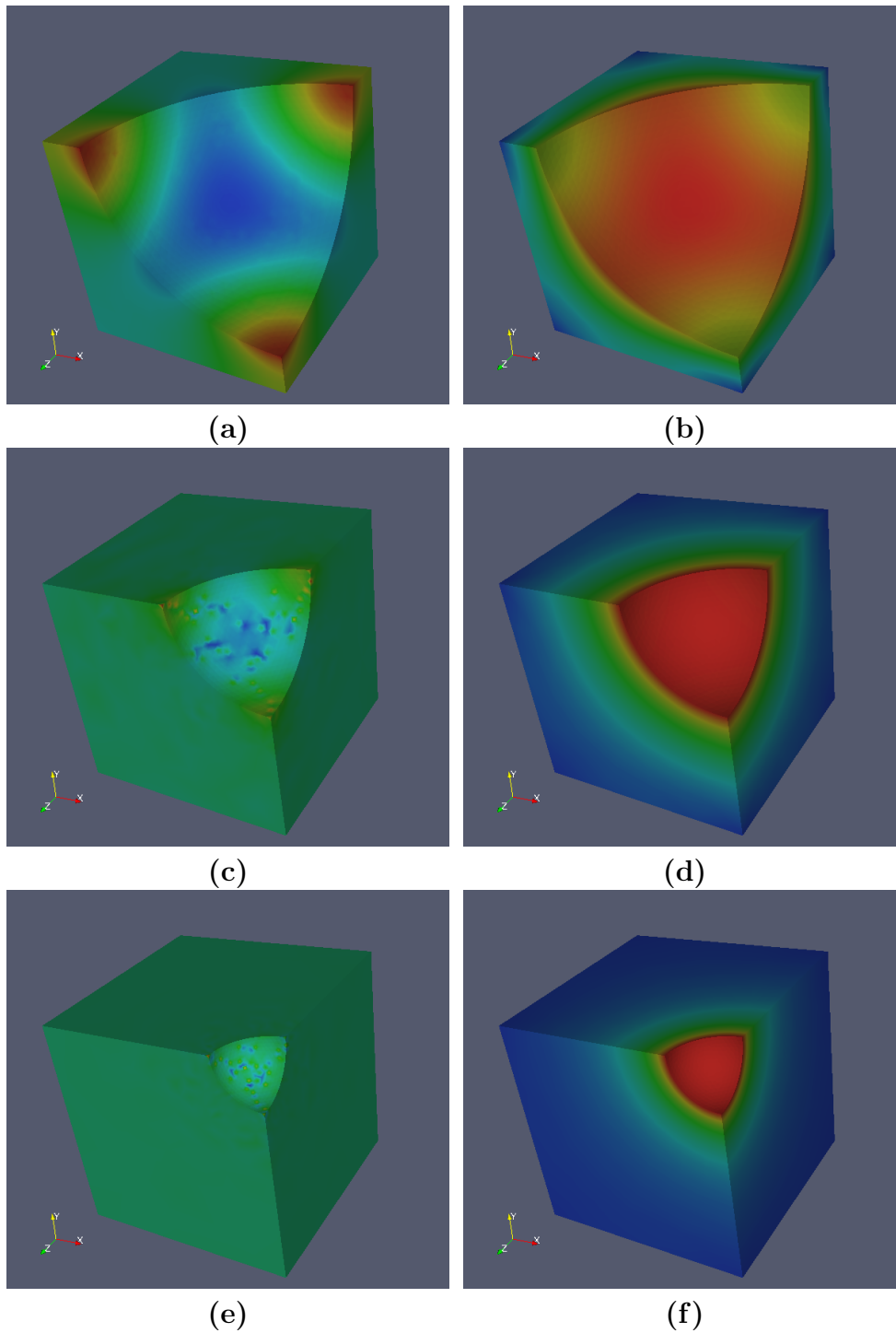


Figure 18. Figures on the left are the pressure fields for domains complementing spheres of radii $a = .40$, $a = .20$, and $a = .10$. Figures on the right are the corresponding velocity magnitude fields.